eLife

Reviewed Preprint
v1 • May 5, 2026
Not revised

For correspondence:
angus.wilson@nyulangone.org

* Joint first authors: contributed equally

# Joint senior authors: contributed equally

Competing interests: No competing interests declared

Funding: See page 26

Reviewing editor: Pedro Batista, National Institutes of Health, National Cancer Institute, United States



# Calibrated analysis framework for nanopore direct RNA sequencing uncovers cell-specific m$^6$A stoichiometry at conserved sites

**Denise Ohnezeit[1,*], Elene Loliashvili[2,*], Gregory Putzel[3], Ruth Verstraten[2,4], Jianheng Liu[5], Luke S Nicholson[5], Alejandro Pironti[3], Samie R Jaffrey[5], Daniel P Depledge[1,2,4,6,#], Angus C Wilson[1,#]**

[1]Department of Microbiology, New York University School of Medicine, New York, United States • [2]Institute of Virology, Hannover Medical School, Hanover, Germany • [3]Antimicrobial-Resistant Pathogens Program, New York University Grossman School of Medicine, New York, United States • [4]German Center for Infection Research (DZIF), partner site Hannover-Braunschweig, , Germany • [5]Department of Pharmacology, Weill Medical College, Cornell University, New York, United States • [6]Cluster of Excellence RESIST (EXC 2155), Hannover Medical School, Hanover, Germany

## eLife Assessment

This **valuable** study compares orthogonal approaches for detecting RNA chemical modifications and provides a helpful framework for improving the reliability of direct RNA sequencing-based identification of RNA modifications. The evidence supporting the technical benchmarking claims is **solid**. However, support for the broader biological conclusions is not as strong, and the quantitative interpretation of the results, as well as the limitations of the underlying models, would benefit from further clarification.

https://doi.org/10.7554/eLife.110672.1.sa3

## Abstract

Nanopore direct RNA sequencing (DRS) coupled with Dorado modification-aware basecalling enables mapping of epitranscriptomic modifications including N$^6$-methyladenosine (m$^6$A) at the level of individual RNAs. However, a lack of systematic benchmarking continues to raise questions regarding the sensitivity, specificity, and reproducibility of this method. To address this and to establish a best-practice workflow, we evaluated multiple Dorado versions using *in vitro* transcribed RNA and an m$^6$A methyltransferase inhibitor as specificity controls. We established that stringent filtering is necessary to reduce false-positive calls and found strong concordance at high-stoichiometry sites when compared to an orthogonal m$^6$A mapping method (GLORI). Further, by applying DRS to human primary fibroblasts and HD10.6 neurons, we uncovered cell type-specific differences in m$^6$A stoichiometry, indicating a finely tuned epitranscriptomic regulation. Our study thus presents the first systematic comparison of Dorado and GLORI from the same input RNA and expands characterization of the m$^6$A epitranscriptome to fibroblasts and neurons.

## Introduction

Epitranscriptomics describes the occurrence of chemical modifications on RNA that regulate stability, localization, splicing, translation or decay (Gilbert and Nachtergaele 2023). To date, over 170 RNA modifications are known to occur across all classes of RNA including eukaryotic mRNA (Cappannini et al. 2023). Of these, at least thirteen different chemical modifications have been characterized in mRNAs, comprising both cap-proximal and internal modifications (Anreiter et al. 2021). By contrast, current evidence indicates that lncRNAs harbor a more limited repertoire of modifications, primarily W$^6$- methyladenosine (m$^6$A), 5-methylcytosine (m$^5$C), and

N7-methylguanosine ($m^7G$) (Yang et al. 2024a). One of the best studied and most abundant internal mRNA modifications is $m^6A$. Functional studies of $m^6A$ methylases, demethylases and $m^6A$ binding proteins, as well as sequencing-based mapping methods have increased our understanding of $m^6A$ as a reversible and dynamic modification that fine-tunes nearly all aspects of mRNA metabolism (Zaccara et al. 2019; He and He 2021; Murakami and Jaffrey 2022; Gilbert and Nachtergaele 2023; Sendinc and Shi 2023).

In addition to $m^6A$, other widespread and functionally important marks include $m^5C$, which is less abundant but influences mRNA export and stability, pseudouridine (ψ), which contributes to mRNA stability, translation and splicing, and adenosine-to-inosine (A to I) editing, which is involved in splicing, stability and recoding events that contribute to protein diversity (Sun et al. 2023).

Techniques based on short-read (Illumina) sequencing have advanced in recent years to achieve single-nucleotide resolution and quantitative mapping of RNA modifications. The approaches that have emerged to map $m^6A$ can be broadly classified as antibody-based, enzyme-assisted or chemical conversion methods (Moshitch-Moshkovitz et al. 2024).

Early antibody-based techniques (Dominissini et al. 2012; Meyer et al. 2012; Linder et al. 2015) provided the first transcriptome-wide insights into $m^6A$ architecture, albeit at limited resolution. Enzyme-assisted methods (Meyer 2019; Xiao et al. 2023) have improved precision but can introduce enzymatic biases. These biases are avoided with GLORI-Sequencing (GLORI), which selectively deaminates unmethylated adenosines, enabling theoretically unbiased, quantitative, single-nucleotide mapping of $m^6A$ (Liu et al. 2023).

Despite advances, the broad utility of these approaches is limited by a lack of isoform specificity, as well as biases associated with amplification, specificity of antibodies or variable adenosine conversion rates (Diensthuber and Novoa 2025). Oxford Nanopore Technologies (ONT) direct RNA sequencing (DRS) offers an alternative to these methods by analyzing native RNA molecules that have retained their modifications (Garalde et al. 2018). As single RNAs pass through nanopores, signal changes are interpreted to determine canonical and modified residues at single-nucleotide resolution on individual transcripts (Jain et al. 2016; Viehweger et al. 2019). For the now discontinued DRS SQK-RNA002 chemistry used with R9 flowcells, multiple research groups developed algorithms for detecting RNA modifications. These methods can be divided into error rate-based and current signal-based (Abebe et al. 2022). While the recent release of the DRS SQK-RNA004 chemistry and RNA-specific flowcells reduced the utility of many of these tools, introduction of a modification-aware basecaller (Dorado) provides an all-in-one toolkit for basecalling, RNA modification detection, and poly(A) tail length estimation. Early versions of Dorado (e.g. v0.5.0 and v0.6.0) enabled $m^6A$ (DRACH-context only) detection, while version v0.7.0 enabled detection of ψ and all-context $m^6A$. More recent versions (v0.8.0 and v0.9.0) allow both DRACH- and all-context $m^6A$ detection, together with ψ, inosine and $m^5C$ (Zou et al. 2025).

In a recent overview of this emerging technology, Cruciani and Novoa highlighted the importance of rigorous evaluation of the limitations of Dorado and advocated forcefully for the establishment of best practices to ensure consistency and accuracy going forward (Cruciani et al. 2025). To date, only a handful of studies of this kind have been published. A series of studies from Novoa and colleagues showed that Dorado performs robustly on synthetic modified and unmodified RNA molecules but also found that overlaps in the identification of specific modifications and false-positive calls remain a challenge but can be mitigated by the inclusion of *in vitro* transcribed (IVT) controls (Cruciani et al. 2025; Diensthuber and Novoa 2025). Independently, Esfahani and colleagues used poly(A) RNA from a B-lymphocyte cell line to compare SQK-RNA002 and SQK-RNAOO4-derived DRS data. While they concluded that Dorado outperformed other RNA modification detection tools, IVT controls were necessary to reduce false-positive calls (Esfahani et al. 2025). Recent benchmarking efforts comparing Dorado and m6Anet on SQK-RNA004 chemistry have shown that both tools achieve high recall and strong stoichiometry correlations at DRACH motifs but exhibit higher false discovery rates on IVT controls and lower recalls of low-stoichiometry genomic $m^6A$ sites. However, these evaluations relied on previously published GLORI and eTAM-Seq datasets, rather than matched input material (Diensthuber and Novoa

2025; Zou et al. 2025). By directly comparing $m^6A$ detection by DRS coupled with Dorado and GLORI on the same RNA inputs, our study overcomes this limitation. Specifically, we systemically benchmark multiple versions of Dorado using poly(A) RNA from primary (normal) human dermal fibroblasts (NHDFs) and functional human neurons produced through terminal differentiation of HD10.6 cells (Raymon et al. 1999), along with IVT RNA. We included treatments with STM2457, an enzymatic inhibitor of the primary $m^6A$ methyltransferase METTL3 (Yankova et al. 2021), to robustly assess false-positive $m^6A$ detection rates and also compared the DRS outputs with those obtained from GLORI (Yang et al. 2024b) using the same RNA as input. While our analysis is centered on the sensitivity and specificity of $m^6A$ detection in DRS datasets, we also benchmark the ability of Dorado to reliably detect $m^5C$, ψ, and inosine. Together, our data provides a robust workflow for DRS-based modification detection that reliably captures transcriptome-wide, isoform-level, site-specific stoichiometries of RNA modifications.By expanding $m^6A$ mapping on primary human fibroblasts and functional human neurons, we uncover mostly conserved $m^6A$ profiles but reveal increased site-specific $m^6A$ stoichiometries in neuronal cells.

# Results

## Systematic benchmarking of ONT's Dorado across human cell types

To evaluate the performance of ONT's basecalling tool Dorado across different human cell types, we selected primary NHDFs and differentiated HD10.6 cells as a neuron-like model. Prior to isolation of total RNA, cells were treated for 48h with a small molecule inhibitor of METTL3 (STM2457) or with vehicle (DMSO). We then isolated poly(A) RNA and subjected the same input material to both DRS and GLORI. The same material was also used to generate IVT RNA (Fig. 1A). Dorado basecalling using version v.0.9.0 resulted in over 13M reads using poly(A) RNA from NHDFs treated with DMSO or STM2457, while we obtained over 5M and 10M reads from DMSO- and STM2457-treated HD10.6 cells, respectively. The rate of primary alignment to the human genome (hg38) was over 98% for all the sequenced samples. A detailed overview of read statistics generated by DRS can be found in Supplementary Table 1.

To systematically benchmark Dorado, we performed basecalling using versions v0.5.0 through v0.9.0. Reads were aligned to the human genome and transcriptome to obtain comprehensive information on isoform-level modification detection. Further, we explored different aspects of detected modifications using the outputs generated by ONT's Modkit tool. We assessed multiple filtering strategies using base and modification probabilities, as well as stoichiometry distributions, and evaluated them based on the IVT data and sensitivity to METTL3 inhibition. By filtering out fa Ise-positive calls using multiple control layers, we determined high-confidence $m^6A$ sites (Fig. IB). Finally, we compared these high-confidence predictions with sites identified by GLORI performed on the same input RNA. Using these results, we developed a benchmarked pipeline that filters $m^6A$ sites predicted by Dorado to minimize false-positive detection without impacting sensitivity (Fig. IC).

## Stringent filtering of modification probabilities removes false positives

During modification-aware basecalling, each nucleotide is assigned a basecall probability score ranging from 0 to 1. Similarly, individual modified nucleotides are assigned a modification probability score in the same range. To establish a baseline for false-positive $m^6A$ predictions, we plotted basecall and modification probability distributions for an IVT poly(A) RNA dataset processed using Dorado v0.9.0 and aligned to human genome (Fig.2). We binned basecall and modification probability values for A and $m^6A$ (all-context and DRACH) and compared this data from DMSO- and STM2457-treated NHDF datasets.

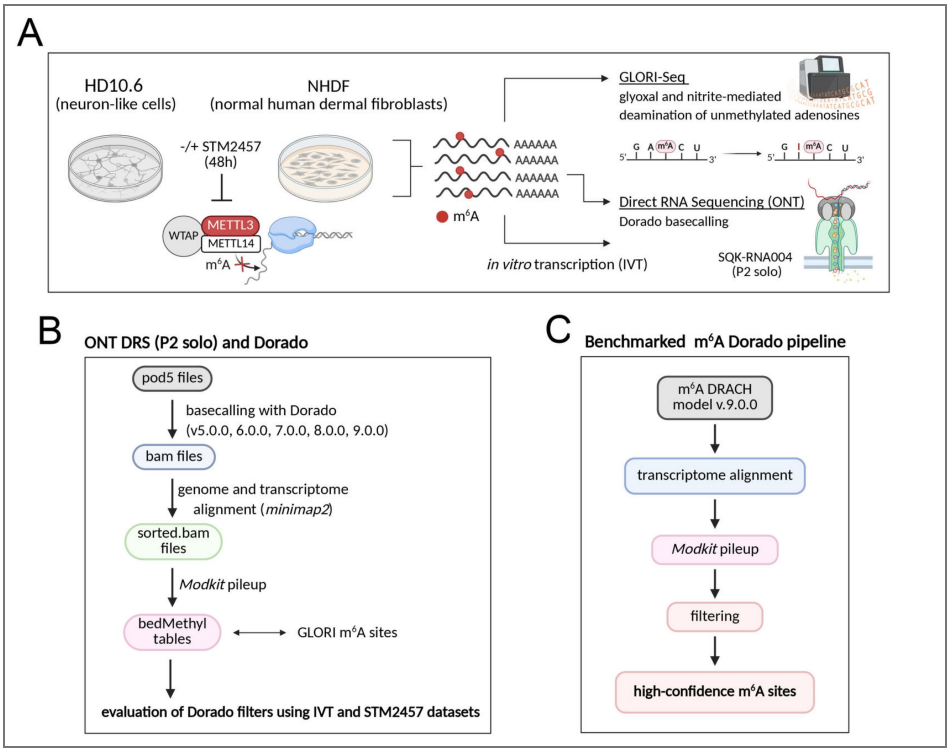


**Figure 1. Workflow for m$^6$A mapping in different human cell types using orthogonal sequencing approaches.**

**(A)** Schematic of the experimental setup. RNA was isolated from NHDFs and differentiated HD10.6 cells treated with STM2457 or DMSO for 48h. Poly(A) RNA was subjected to DRS and GLORI from the same input material. IVT RNA was generated in parallel to assess potential false-positive modification calls. **(B)** Workflow for benchmarking Dorado basecalling. Reads were processed with Dorado versions v.0.5.0 through v0.9.0, aligned to the human genome or transcriptome, and analyzed with ONT's Modkit tool. Multiple filtering strategies were tested against IVT controls and METTL3 inhibition (STM2457). Resulting m$^6$A sites were compared with GLORI data from the same input RNA. **(C)** Final benchmarked Dorado pipeline to detect high confidence m$^5$A sites.

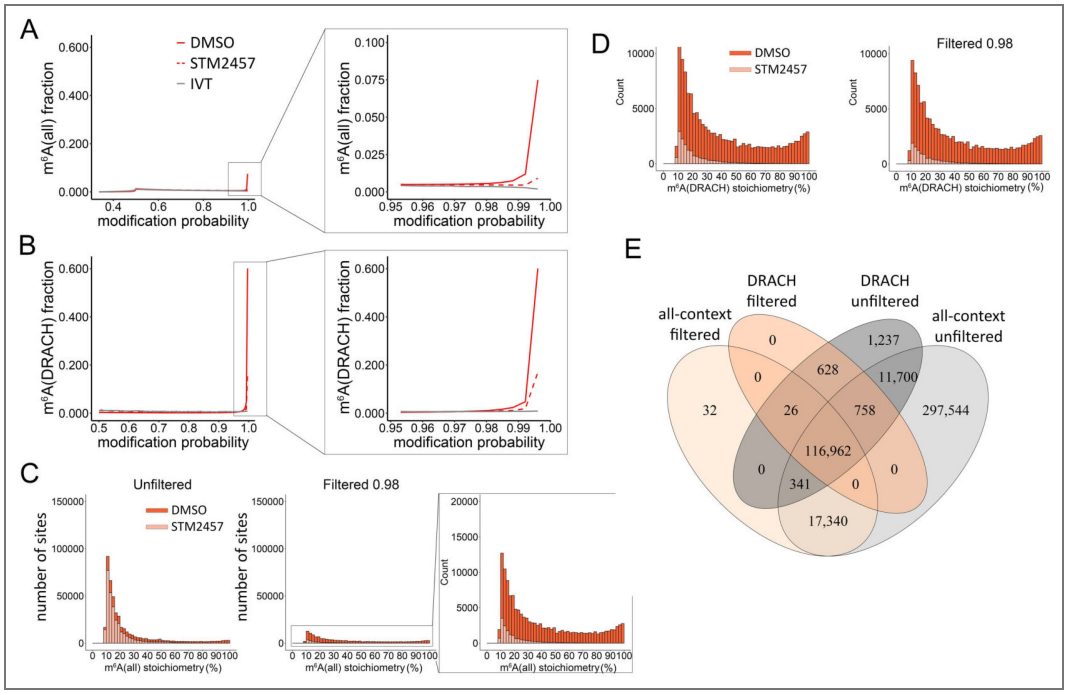


**Figure 2. Modification probability of 0.98 and stoichiometry score of > 10% are necessary cutoffs to identify m$^6$A sites accurately.**

**(A)** Dorado v0.9.0-generated modification probability distributions for all-context m$^6$A from genome-aligned DMSO- and STM2457-treated NHDFs plotted against the ones from IVT NHDF poly(A) RNA. DMSO probability score distribution is shown as a red solid line, STM2457 - red dashed line, IVT - grey solid line. **(B)** Same as in (A), but for DRACH-context m$^6$A sites. **(C)** Stoichiometry (> 10%) distributions for all-context π?Afrom DMSO- (in red) or STM2457-treated (in pink) NHDF datasets (genome-aligned) are plotted using a 0.98 modification probability cutoff and a filter for > 20 reads. **(D)** Same as in (C), but for DRACH-context m$^6$A sites. **(E)** Overlap of m$^6$A sites between all-context and DRACH models (A basecall accuracy > 80%, coverage > 2Oreads, stoichiometry > 10%), comparing non-filtered to filtered (modification probability > 0.98) outputs. **(F)** Metagene plots showing the density of m$^6$A (all-context - dark red, DRACH-context - bright red) sites across all annotated poly(A) transcripts (left) and monoexonic poly(A) transcripts (right) from genome-aligned DMSO-treated NHDF datasets filtered with 0.98 modification probability, > 20 coverage and > 10% stoichiometry.

We observed that 75-90% of A basecalls (in all datasets) have probability scores above 0.8 (Fig. S1A). Since all A bases are considered during all-context $m^6A$ calling, the fraction of $m^6A$ sites is substantially smaller when compared to DRACH-context $m^bA$ sites (Fig.2A,B, Fig.S1B,C). The modification probability distributions are effectively identical for DMSO-treated, STM2457-treated and IVT datasets below 0.98, while the profiles differ substantially at probabilities > 0.98. This suggests that sites detected below 0.98 are likely false positives, indicating that only high-probability $m^6A$ calls can be considered reliable. Here, STM2457 treatment shows a marked reduction in the number of reported $m^6A$ sites in both all-context and DRACH-only datasets when compared to the DMSO treatment (Fig. 2A,B).

In addition to $m^6A$, we examined modification probability distributions for ψ, inosine and $m^5C$, each of which can be basecalled with Dorado v0.9.0 (Fig. S2). For ψ and I, the modification probability distributions for the STM2457 and DMSO datasets only diverge from the IVT dataset at > 0.99 modification probability, thus providing a relevant threshold for filtering out false positives (Fig. S2A,B). By contrast, $m^5C$ modification probability distributions were similar between all three datasets and no filter could be adequately established (Fig. S2C). While this likely reflects a low rate of $m^5C$ installation, it also indicates that the $m^5C$ model utilized by Dorado requires further refinement.

Modification probability distributions have similar profiles fortranscriptome-aligned NHDF data (Fig. S3) as well as genome- and transcriptome-aligned data from HD10.6 cells (Fig. S4, Fig. S5). Of note, the fraction of high-probability inosine sites is increased in STM2457-treated cells, compared to DMSO-treated ones in genome-aligned data (Fig. S2B, Fig.S4D), which points to increased numbers of retained introns in the METTL3-inhibited sample. Accordingly, this effect is absent in transcriptome-aligned data (Fig. S3D, Fig. S5D).

While IVT transcriptomes serve as excellent negative controls, we also considered whether the RNA calibration strand (RCS) that is added during DRS library preparation could serve a similar function. The RCS is a synthetic Enolase II RNA derived by IVT[13] that, similarly to the IVT transcriptomes, are devoid of RNA modifications. Despite the reduced diversity of sequence in the RCS data, the overall results were comparable to that from the IVT transcriptome data (Fig. S6A,B, Fig. 2A,B), demonstrating that the RCS can be used as a "built-in" negative control for modification detection with DRS. Finally, we determined that basecall and modification probability distributions remain generally consistent between Dorado versions although more $m^6A$ and ψ sites are detected with high modification probability in Dorado versions v0.8.0/v0.9.0 compared to v0.7.0 (Fig. S6C-E).

## Filtering by stoichiometry further eliminates potential false positives

We next examined the stoichiometry distributions for all $m^6A$ sites in both unfiltered and filtered NHDF datasets (Fig. S7). Here, unfiltered datasets showed that the vast majority of $m^6A$ sites, 92% for all-context and 75% for DRACH-context, have stoichiometry values < 10% with less than 1% sites showing high (> 50%) stoichiometry. Application of our filtering strategy removed over 70% of the sites (Fig. 2E), regardless of the context, almost all of which showed stoichiometries of < 10%, without significantly changing the numbers of high stoichiometry sites detected (Fig. S7). A similar analysis of the IVT transcriptome revealed large numbers of false positive $m^6A$ sites with stoichiometry values below 10%, most of which were eliminated by application of our filters (Fig. S8A,B). However, the remaining presence of low stoichiometry false-positive sites indicates that an additional layer of filtering to exclude sites with < 10% stoichiometry is beneficial. An additional argument in support of our modification probability filtering strategy is the observation that treatment with the METTL3 specific inhibitor STM2457 dramatically reduced $m^{\acute{r}}A$ installation at sites with > 10% stoichiometry in untreated datasets in a context-independent manner (Fig. 2C,D, Supplementary Table 2). Similar results were observed for the transcriptome aligned NHDF and HD10.6 $m^6A$ stoichiometry distributions as well (Fig. S9, Fig. S10, Supplementary Table 2).

To determine whether our filtering strategy could be applied to other RNA modifications detected by Dorado, we generated stoichiometry distributions for ψ and inosine in unfiltered and filtered (> 0.99 modification probability) human genome-aligned DMSO- and STM2457-treated NHDFs and HDlO.6s. As with $m^6A$ (Fig. S7), 92% of detected ψ and 96% of inosine have less than 10% stoichiometry (Fig. S11, Fig. S12). A recent study that explores ψ in human mRNAs using 2-bromoacrylamide-assisted cyclization sequencing (BAGS) corroborates our results, showing that 82% of ψ modifications are detected at low levels (below 20%) (Xu et al. 2024).

Above 10% stoichiometry, in our data, there are more inosine sites in STM2457-treated cells than DMSO-treated cells, reflected also in the stoichiometry distributions (Fig. S11, Fig. S12, Supplementary Table 2). ψ and inosine stoichiometry distributions in our IVT data (Fig.S8C,D) further validates our filtering strategy of > 0.99 modification probability, as it substantially reduces the number of detected false-positive sites in the unfiltered data even at higher (> 50%) stoichiometries in case of inosine (Fig.S8D).

We have thus demonstrated that setting thresholds for basecall modification probabilities provides a robust method for identifying and filtering false-positive modification calls. For the purposes of this

study, we further evaluated the effect of placing the modification threshold on the modification data and restricted the downstream analyses to $m^6A$ sites with probability scores > 0.98.

## RNA modification detection rates differ between Dorado versions

Dorado basecalling relies on models generated using Remora (*github.com/nanoporetech/remora*) that are frequently updated. This raises an important question as to whether these updates produce notably different outputs that could impact biological interpretation. To address this, we utilized multiple Dorado versions and Remora models to perform modification calling of our NHDF dataset. We restricted our analyses to $m^6A$ and ψ as these are the only modifications that could be detected in previous versions. Here, we observe that $m^6A$ and ψ stoichiometry distributions are generally consistent between different Dorado versions (Fig. S13), albeit with greater numbers of low stoichiometry (< 10%) sites detected in older Dorado versions. There is a large overlap of the detected > 1%-stoichiometry $m^6A$ (DRACH and all-context) and ψ sites between versions, although there are a lot of unique all-context $m^6A$ and ψ sites identified with just v0.7.0 and not v0.8.0-v0.9.0, that are reduced after applying our modification probability filter (Fig. S14A,B). ψ sites uniquely detected with different versions are found in slightly different sequence contexts (Fig. S14C,D). Thus, while RNA modification detection with Dorado is sensitive to changes in the underlying models/versions, this can be effectively controlled through the application of filters that only retain sites with high-confidence modification probability calls.

## GLORI exhibits reduced specificity but converges with Dorado predictions at high stoichiometry sites

To assess the agreement of DRS Dorado-derived predictions with an orthogonal $m^6A$ detection method, we conducted GLORI on the same NHDF RNA preparations. To ensure a fair comparison of $m^6A$ sites across the two methods, we applied the following filtering strategies: For Dorado (DRACH model), this included thresholds on modification probability (A > 0.8, $m^6A$ > 0.98) and read coverage (> 20). For GLORI, we used filters based on coverage (> 20) and statistical significance (p-value < 0.05). Next, we extracted $m^6A$ sites that were present in both DMSO and STM2457 treated samples and removed all sites with < 10% stoichiometry in DMSO (Fig. 3A). This stepwise strategy reduced false positives and enabled a fair comparison of the high confidence $m^6A$ sites identified by both approaches.

As shown in the violin plots, both the all-context and DRACH-context Dorado models identify similar numbers of $m^6A$ sites (81,012 (all-context model) and 72,372 (DRACH model)), the stoichiometries of which were strongly reduced upon STM2457 treatment (Fig. 3B). When we analyzed the motifs of the $m^6A$ sites detected with the all-context model, we observed nearly 9,000 sites outside of DRACH motifs.

Importantly, the total number of $m^6A$ sites within DRACH motifs was nearly identical to the number of $m^6A$ sites reported using the DRACH model (Fig.3B). Unexpectedly, GLORI detects a substantially higher number of sites when using all motifs (140,934) compared to DRACH motifs alone (27,926) (Fig. 3C). The fact that most GLORI-identified sites fall outside DRACH motifs suggests these are false positives. This interpretation is reinforced by the observation that the overlap between Dorado and GLORI datasets remains virtually unchanged when comparing GLORI "all motif" and "DRACH motifs" (n=l3,6l4) site sets, underscoring that the additional non-DRACH sites in GLORI (n= 113,008) are largely spurious (Fig. S15A).

We obtained similar results when comparing $m^6A$ sites obtained with Dorado and GLORI from HD10.6 cells. Overall, we detected a similar number of $m^6A$ sites in HD10.6 cells using the all-context and DRACH-specific Dorado models (77,728 and 67,222, respectively) (Fig. S15B). By contrast, we detected 174,282 vs 27,965 $m^6A$ sites using GLORI without or with DRACH filtering, respectively (Fig. S15C).

To evaluate how stoichiometry thresholds affect the agreement between GLORI and Dorado, we compared the overlap of high-confidence GLORI-identified sites with Dorado $m^6A$ (DRACH context) calls across increasing $m^6A$ stoichiometry cutoffs (Fig. 3D). At the lowest stoichiometry threshold applied (> 10%), 13,614 sites overlapped, representing less than half (48.8%) of GLORI sites. However, as the stringency increased, the relative overlap increased sharply: at > 20%, nearly 70% of GLORI sites overlapped (11,536 sites), at > 50% almost 90% overlapped (6,307 sites), and at the highest cutoff (> 80%), over 93% of GLORI sites (3,119 sites) were also detected by Dorado. These results demonstrate that while GLORI detects a broad set of potential $m^6A$ sites, only the sites with high stoichiometries overlap with Dorado, indicating high signal to noise ratios in the GLORI datasets.

GLORI relies on the high-efficiency conversion of adenosine to inosine with overall gene A to I conversion rates needing to exceed 95-98% (Xu et al. 2024; Xie et al. 2025). Similarly, we observed the conversion rates for our NHDF and HD10.6 datasets to be 95% (Supplementary Table 3), but we found that small variations in gene conversion rates can strongly influence the sensitivity and specificity of GLORI, as only high-stoichiometry $m^6A$ sites overlapped with DRS-derived predictions (Fig. 3D).

## DRS coupled with Dorado outperforms GLORI in isoform-specific $m^6A$ detection

Next, we wanted to highlight the advantage of long-read sequencing in terms of mapping reads with isoform-precision to the human transcriptome, which is not possible using GLORI due to its reliance on short-read sequencing. We first confirmed that mapping Dorado-basecalled sites to the human transcriptome results in the detection of similar numbers of $m^6A$ sites in both NHDFs and HD10.6 cells (Fig. S15D,E). To assess if DRS coupled with Dorado identifies distinct $m^6A$ profiles on different transcript isoforms, we analyzed the *SPEN* gene locus which was previously shown to contain more than 100 $m^6A$ sites (Liu et al. 2023). On a genomic level, we detected 42 $m^6A$ sites using DRS, while GLORI only detected 5 $m^6A$ sites (Fig. 3E). Out of the 7 total isoforms of *SPEN*, *SPEN-201* and *SPEN-202* were detectable in DRS-derived data, considering a minimal coverage of 20 (Supplementary Table 4). When plotting the $m^6A$ sites detected by transcriptome-aligned DRS data, we found that the *SPEN-201* isoform exhibited more $m^6A$ sites, albeit with a lower median stoichiometry compared to the *SPEN-202* isoform (Fig. 3F). This example highlights that DRS is superior compared with GLORI for isoform-level $m^6A$ quantification.

## Dorado profiling reveals cell type differences in $m^6A$ distribution and stoichiometry

To assess the reproducibility of Dorado across DRS datasets derived from different cell types, we compared the $m^6A$ methylomes of NHDFs and HD10.6 cells. To ensure a fair comparison, we extracted genes that were expressed in both cell types. Next, we compared the total numbers of

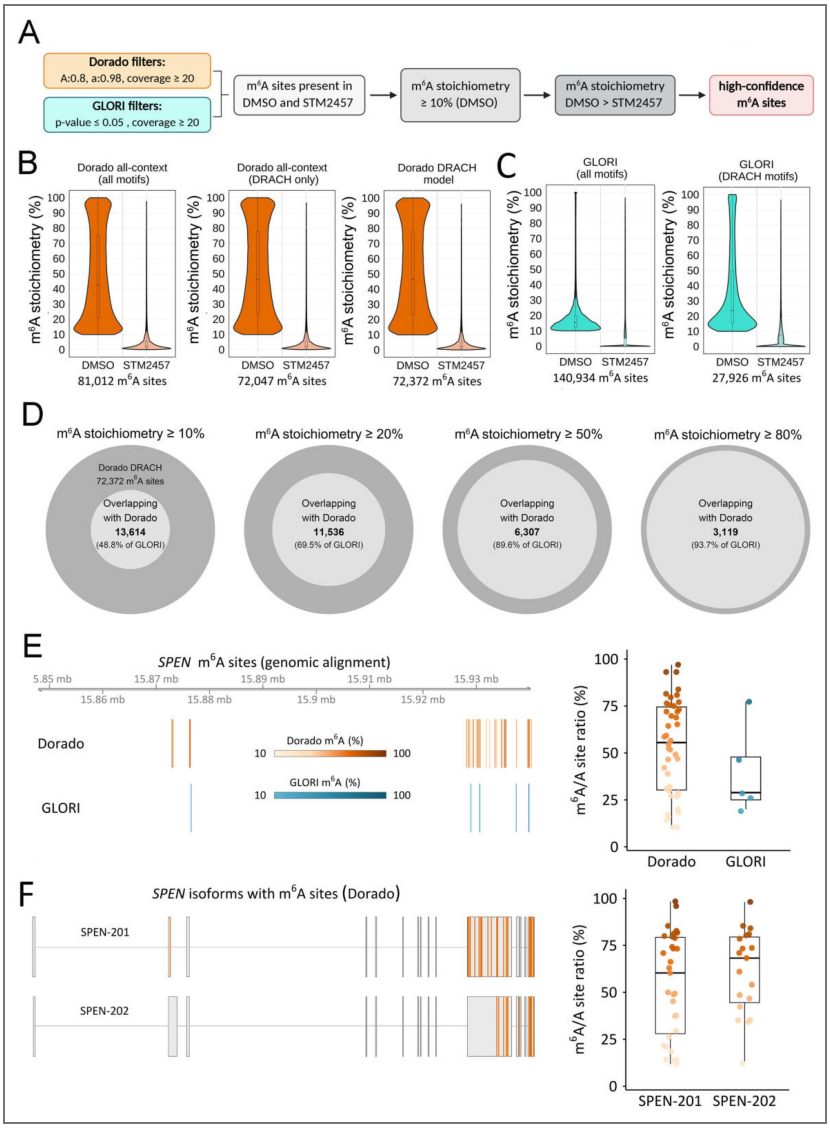


**Figure 3. Comparison of m$^6$A sites detected by Dorado and GLORI.**

**(A)** Filtering strategy for Dorado vs GLORI to obtain a high-confidence list of m$^6$A sites in NHDFs. **(B)** Stoichiometry distributions are plotted from genome-aligned DMSO- or STM2457-treated NHDF datasets using the indicated Dorado models and the filtering strategy shown in (A). **(C)** Stoichiometry distributions from GLORI performed on DMSO- or STM2457-treated NHDFs are plotted, using the filtering strategy shown in (A). In addition, m$^6$A sites were filtered for DRACH motifs (right plot). **(D)** Overlap of high confidence m$^6$A sites detected by Dorado vs GLORI. GLORI datasets were filtered using increasing m$^6$A stoichiometry cutoffs (from left to right). **(E)** m$^6$A sites in the *SPEN* gene detected by GLORI and Dorado. Boxplots (right) represent the m$^6$A stoichiometries per m$^6$A site shown on the left. **(F)** *SPEN* isoforms with m$^6$A sites, determined by Dorado. Boxplots (right) show the distribution of m$^6$A stoichiometries on the m$^6$A sites on *SPEN-201* and *SPEN-202*.

high confidence m$^6$A sites in NHDFs and HD10.6 cells within the genes expressed in both cell types and found that 87% of HDlO.6-derived m$^6$A sites overlap with those detected in NHDFs (Fig. 4A). Site-specific m$^6$A stoichiometries from the shared gene set correlated strongly across cell types (Pearson r = 0.93), although we observed a global shift in the HD10.6 dataset, where m$^6$A stoichiometries were generally higher than in NHDFs (Fig. 4B). Plotting the m$^6$A stoichiometry distributions of the 38,217 m$^6$A sites shared between both cell types showed a strong increase in the median m$^6$A stoichiometry of HD10.6 cells (70.2%), compared to NHDFs (54%) (Fig. 4C).

We next aimed to conduct a comparative motif analysis of m$^6$A sites detected in NHDFs and HD10.6 cells. Sequence logos confirmed strong enrichment of the canonical DRACH consensus motif for both cell types in modification probability-filtered data, with the GGACU pentamer being the most prominent (Fig. 4D,E, Fig.Sl6). Quantification of 5-mer distributions revealed highly similar motif preferences across datasets. While the global motif architecture of m$^6$A deposition is conserved between NHDFs and HD10.6 cells, we observed a trend toward higher stoichiometries in the HD10.6 dataset, particularly within the most abundant DRACH motifs, suggesting enhanced modification efficiency in the neuron-like context (Fig. 4F, G).

Metagene analysis showed, as known previously, that m$^s$A is enriched near the stop codons and in the 3' UTRs (Fig. S17A). Several studies have examined the relationship between exon architecture and m$^6$A distribution on mRNAs[1,2,3], and so we also examined m$^6$A sites in monoexonic transcripts separately and found that monoexonic transcripts are more broadly m$^6$A-modified across entire CDS (Fig. S17A). m$^6$A (both all-context and DRACH-context) distribution profiles look less typical for all-stoichiometry or< 10% stoichiometry sites in both NHDF and HD10.6 datasets (Fig. S17B+C). For all-context m$^6$A (Fig. S17B), modification filter also proves to be deciding for the distribution profile, together with > 10% stoichiometry.

To connect shared m$^6$A sites with their functional context and illustrate their distribution on individual transcripts, we conducted a KEGG pathway analysis with the genes that contain shared m$^6$A sites between NHDFs and HD10.6 cells. We observed a significant enrichment in pathways related to neurodegeneration, infection, and intracellular signaling, including axon guidance and mTOR signaling (Fig. 4H). To further illustrate these findings, we examined representative genes contained in one or more of these pathways. *WNTB5*, *MAPK1*, *AKT1*, *NCK1* and *NRP1* all showed robust methylation in both NHDFs and HD10.6 cells, with consistently higher stoichiometries observed in the neuronal-like context. In contrast, *ACTG1*, included as a housekeeping control not represented in the enriched pathways, displayed stable and comparatively uniform methylation across both cell types (Fig. 4I).

Together, these results demonstrate that while the global architecture of m$^6$A deposition is largely conserved between primary fibroblasts and neuronal-like cells, but unexpectedly the neuronal context is characterized by a global shift toward higher m$^b$A stoichiometries. This difference is readily detectable in single genes. These findings suggest that cell type-specific regulation of m$^6$A may fine-tune core cellular pathways relevant to that cell type.

# Discussion

High rates of false positives remain a major problem in epitranscriptomic mapping tools, even with the advent of modification-aware basecalling models (Cruciani et al. 2025). Comparing the outputs of orthogonal methods performed on the same input material, combined with use of IVT RNA and/or specific methyltransferase inhibition, offers an effective mitigation strategy (Cruciani et al. 2025; Diensthuber and Novoa 2025). The results presented here establish a robust framework that minimizes false positives and enables isoform-specific and quantitative m$^6$A mapping. Through a direct comparison with GLORI, we showed that combining DRS datasets with Dorado modification-aware basecalling provides greater scalability, isoform resolution, and reproducibility across different cell types. Further, the simplicity of DRS library preparation enhances consistency whereas GLORI is constrained by a laborious and technically challenging protocol that is extremely sensitive to adenosine conversion rates (Shen et al. 2024). Despite these limitations, we determined that the majority of m$^6$A sites in our filtered DRS datasets could

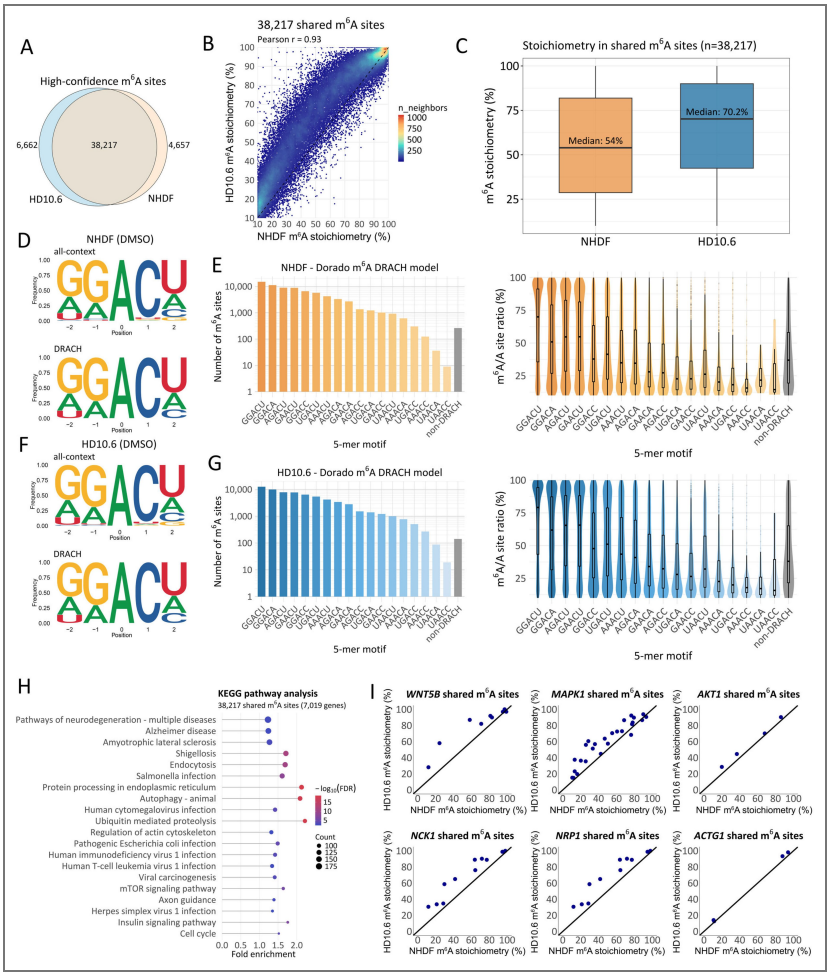


**Figure 4. Comparative analysis of m$^6$A modification patterns in NHDFs and HD10.6 cells using Dorado v0.9.0.**

**(A)** Overlap of high confidence m$^6$A sites between NHDFs and HD10.6 cells. **(B)** Correlation of shared m$^6$A stoichiometries (n=38,2l7). **(C)** Boxplots showing the m$^6$A stoichiometry distributions of the 38,217 detected in both NHDFs and HD10.6 cells. **(D+E)** Motif analysis showing m$^6$A (all-context and DRACH-context) motif logos, 5-mer distributions and modification stoichiometries in NHDFs. **(F+G)** Same as in (D+E) but for HD10.6 cells. (H) KEGG pathway analysis (DAVID Bioinformatics Resources) of shared m$^6$A-containing genes. (I) m$^6$A stoichiometries of representative examples of individual genes from enriched pathways **(H)**. *ACTG1* serves as a housekeeping control.

be confirmed by GLORI. By expanding our analysis across multiple human cell types, we further determine that the sites of $m^6A$ installation are conserved for the most part but that the stoichiometries show cell-type specific differences.

Crucially, the inclusion of transcriptome-wide IVT datasets and the use of a selective METTL3 inhibitor (STM2457) provides a robust approach to developing filters that dramatically decrease false-positive $m^6A$ detection. The impact of both approaches was readily visualized by plotting modification probability distributions, enabling our determination that retaining only $m^6A$ calls with confidence scores of 0.98 or greater retained almost all STM2457-sensitive $m^6A$ sites while eliminating the large numbers of false-positive $m^6A$ sites reported for the IVT datasets. This approach is supported by a recent study which highlighted that Dorado introduces large numbers of false positives outside canonical DRACH contexts (Xie et al. 2025). Our data confirms that in the unfiltered datasets, the number of false positives is higher in the all-context model compared to the DRACH model. This may reflect the degenerate nature of the canonical DRACH consensus and understudied differences in sequence preference between different cell types and organisms. Retaining only sites at which $m^6A$ stoichiometries exceeded 10% further reduced false-positive rates while also focusing the results on identification of sites that are more likely to be biologically significant. The combined effect of these filters was to provide a strong agreement between the $m^6A$ all-context and $m^6A$ DRACH model in the detection of high confidence $m^6A$ sites, as observed by filtering for DRACH motifs from $m^6A$ sites detected with the all-context model (Fig.3B).

Prior studies have emphasized the need for isoform-resolved $m^6A$ quantification by demonstrating widespread heterogeneity in $m^6A$ levels between genes and their isoforms (Guo et al. 2025; Xie et al. 2025). Here, we showed that aligning DRS datasets to the human transcriptome reveals differential $m^6A$ installation patterns between isoforms, underscoring the importance of accurate, isoform-specific $m^6A$ quantification at single-molecule resolution and highlighting the advantage of DRS against short-read sequencing approaches such as GLORI (Fig. 3E,F).

Recently, the ability of Dorado and m6Anet (Hendra et al. 2022) to identify $m^6A$ in DRS datasets from 293T and HeLa cells were systematically evaluated using IVT RNA and comparisons to published datasets obtained by GLORI and eTAM-seq (Zou et al. 2025). In this case the authors found that Dorado (v0.7.2) outperforms m6Anet but also advocated for the importance of applying filters to reduce false positive calls. Likewise, we found that IVT RNA served as a valuable negative control to detect false positive calls. Furthermore, using the RNA calibration strand (RCS) as a negative control provided a convenient and simpler alternative to IVT RNA, yielding comparable probability distributions and thereby enabling a built-in control for routine experiments (Viehweger et al. 2019). While $m^6A$ detection was generally reproducible across Dorado versions, model-specific differences are present, i.e. v0.7.0 produces substantially more low-confidence all-context $m^6A$ and ψ calls than v0.8.0-0.9.0, highlighting that the models remain under active development and that benchmarking should be repeated when switching to a new model. Recent work further highlights that continued improvements in both nanopore sequencing chemistry and basecalling models significantly enhance RNA modification detection accuracy, emphasizing the importance of revisiting benchmarking and filtering strategies as models evolve (Hewel et al. 2025).

Focusing on other modifications that are detected by Dorado, we observe that inosine and ψ detection appears robust when applying similar filtering strategies as for $m^6A$, the latter supported by other studies (Esfahani et al. 2025; Verstraten et al. 2025). For inosine, we observed an enrichment of high-probability (> 0.99) inosine sites in genome-aligned data from STM2457-treated samples. Further studies are needed to determine whether this reflects increased intron retention or misclassification of modifications by the current inosine model. While DRS is the only approach that allows for robust isoform-specific $m^6A$ mapping, comparisons with orthogonal approaches remain essential to validate findings. When comparing Dorado and GLORI using the same input RNA, we unexpectedly observed that only 50% of $m^6A$ sites with stoichiometries above 10% that were identified by Dorado were also present in the GLORI data although increasing the stoichiometries led to increased overlap (Fig.3D). We attribute this to a

sub-optimal gene-wide adenosine conversion rate of 95% during GLORI, compared to the 98-99% rate reported in the original study (Shen et al. 2024). Here, unconverted adenosines result in high signal-to-noise ratios which result in lower sensitivity, explaining why the overlap with Dorado increases at higher-stoichiometry sites. This is also reflected in the relatively high amount of false positive sites detected outside of DRACH motifs in the GLORI datasets (Fig. 3C). The sensitivity of GLORI to small fluctuations thus limits its utility in comparison to DRS. Whether this can be resolved with improvements to the GLORI methodology (Sun et al. 2025) requires further study.

Prior analyses of $m^6A$ stoichiometry distributions across immortalized human cell lines, including cancer cell lines, have revealed broadly similar $m^6A$ stoichiometry distributions (Guo et al. 2025). By contrast, our analysis of primary fibroblasts (NHDFs) and neuronal cells (differentiated HD10.6 cells) revealed an overall increase in $m^6A$ stoichiometries in neurons compared to fibroblasts, especially in genes associated with neuronal function. While further studies are warranted to establish the underlying mechanisms and functional consequences of these differences, this aligns with the importance of $m^6A$ in neuronal function (Yu et al. 2021). This includes $m^6A$ maps from synaptic and nuclear RNA isolated from mouse dorsal hippocampus which showed that synapse-specific RNAs showed generally higher methylation levels (Sun et al. 2025). Intriguingly, neuronal regulation pathways utilize differentially spliced isoforms (Su et al. 2018) and a recent study revealed isoform-specific differences in $m^6A$ sites and stoichiometries in the human brain that are linked to $m^6A$ machinery expression and cell type context (Gleeson et al. 2025).

In summary, using matched RNA samples from different experimental conditions and from different human cell types analyzed with both Dorado and GLORI orthogonal methodologies, we establish a robust pipeline for the precise and quantitative transcriptome-wide detection of $m^6A$ in DRS datasets. Future studies should aim at extending this approach using orthogonal sequencing approaches to benchmark Dorado-based detection of ψ, $m^5C$ and inosine, as well as the newly released models for 2'O-methylation.

# Methods

## Cell culturing and STM2457 treatment

NHDFs (Lonza) were cultured in Dulbecco's Modified Eagle Medium (DMEM, Gibco), supplemented with 5% heat-inactivated FBS (HI-FBS, Gibco) and 1% penicillin-streptomycin (PS, Lonza) under standard culture conditions. The HD10.6 cell line was originally derived from fetal human dorsal root ganglia (DRG) and immortalized by overexpression of the v-myc oncogene under tetracycline regulation. Upon addition of tetracycline and neurotrophins, these cells can be differentiated into neuron-like cells that show typical neuronal morphology and nociceptive properties(Raymon et al. 1999). For our experiments, we used HD10.6 cells that have been matured for 10 days. For maintenance of undifferentiated HD10.6 cells (a gift from Anna Cliffe, University of Virginia School of Medicine), T-75 flasks were coated with 17 µg/mL fibronectin in PBS for 15 min at 37°C before adding the cell suspension. Cells were grown in Advanced DMEM/F12 (Gibco), supplemented with lx Neurocult SMI (STEMCELLTechnologies), 2 mM L-glutamine (Gibco), lx Primocin (Invivogen) and 10 ng/mL prostaglandin El (Sigma). 0.5 ng/mL bFGF (PeproTech) were added freshly to each media change. For maturation, HD10.6 cells were seeded at a density of 25.000 cells/$cm^2$ in 6-well plates which were pre-coated overnight with 50 µg/mL poly-L-ornithine hydrobromide (Sigma) in 0.5M borate buffer pH 8.5 (Boston Bioproducts), and 1 µg/mL fibronectin (overnight). After cell attachment overnight, media was changed to Neurobasal media (Gibco), supplemented with lx Neurocult SMI, 2mM L-glutamine, lx Primocin, 1 µg/mL doxycycline, 50 ng/mL NGF (Alomone Labs), and 25 ng/mL CNTF, GDNF and NT-3 (PeproTech). Media was changed every three days until HD10.6 cells showed complete neuronal morphology after 12 days. NHDFs and matured HD10.6 cells were treated with 30 µM STM2457 (Sigma) or DMSO for 48h, harvested in TRIzol (Invitrogen), and stored at -80°C until RNA isolation.

## RNA isolation

RNA was extracted by the TRIzol method according to the manufacturer's instructions. Briefly, 0.2 mL chloroform per 1 mL TRIzol were added and mixed by vortexing. After centrifugation for 30 min at l2,OOOxg at 4°C, the aqueous phase was transferred to isopropanol (0.5 mL per 1 mLTRIzol), mixed and incubated for 10 min at room temperature. Subsequently, the samples were centrifuged for 10 min at l2,OOOxg at 4°C and the RNA pellets were washed twice in 75% fresh ethanol. After air-drying for 5-10 min, RNA was dissolved in nuclease-free $H_2O$ and stored at -80°C until further processing. One third of each sample was used for DRS and the remaining same-input material was processed for GLORI. For both DRS and GLORI, poly(A) RNA was selected using the Dynabeads™ mRNA Purification Kit (Invitrogen), according to the manufacturer's instructions.

## GLORI-Sequencing

GLORI reactions were largely performed following the published protocol for RNA protection, deamination and deprotection with several minor adjustments (Shen et al. 2024). Briefly, poly(A) RNA was fragmented at 94°C for 2 min (NEB E6150S) and subjected to glyoxal protection, sodium-nitrite-mediated deamination (750 mM $NaNO_2$ at 16°C for 8h and 4°C for 6h), and deprotection in triethylammonium acetate-formamide buffer at 95°C for 10 min. Library construction was conducted using a ligation-based strategy as described by Liu and colleagues incorporating 5'adapters with 11-nt UMIs(Liu etal. 2025).

Indexed libraries were amplified with NEBNext Dual Primers Set 2 (E778OS), purified using AMPure XP beads, and validated on an Agilent TapeStation (D1000 High Sensitivity). Sequencing was performed on an Illumina NovaSeq 6000 platform (150 bp paired-end mode; >80 million reads per sample).

For data processing, we employed the same computational pipeline described in Liu et al (Liu et al. 2025), but implemented within a Snakemake-based framework that automates the complete analysis starting from raw fastq files (Koster and Rahmann 2012). Details on software versions, workflow availability, and repository links are provided in the Data and code availability section below.

## Generation of a transcriptome-wide IVT RNA library

We sequenced the IVT RNA from both NHDFs and HD10.6 cells along with the native poly(A) RNA to evaluate potential false-positive predictions by Dorado. This was achieved by converting the poly(A) RNA to cDNA using a poly(A) primer and a T7-incorporating strand switch primer and using the cDNA as a template for IVT synthesis.

## Nanopore Sequencing of poly(A) RNA

250-300 ng of isolated poly(A) RNA and 25 ng RNA calibration strand (RCS) were used as input for the standard DRS SQK-RNA004 protocol. Resulting libraries were loaded onto individual PromethlON RNA flow cells before sequencing on the PromethlON 2 Solo instrument for 48h.

## Nanopore basecalling

Basecalling was performed using Dorado v0.5.0, v0.6.0, v0.7.0, v0.8.0 and v0.9.0 (ONT) in super accuracy mode with modification detection enabled for $m^6A$ (DRACH context) in v.0.5.0, 0.6.0, 0.8.0 and 0.9.0, $m^6A$ (all context) in v0.7.0, 0.8.0 and 0.9.0, ψ in v0.7.0, v0.8.0 and v0.9.0, and inosine and $m^5C$ in v.0.9.0. Each dataset was processed with adapter trimming. Resulting unaligned BAM files were converted to FASTQ files containing modification tags for every read in the FASTQ read headers, using SAMtools vl.18 (Li et al. 2009) *[samtools fastq -TMM,ML],*

## Genome and transcriptome level alignments

For genome-level alignment, reads were aligned against a combined human genome reference (GRCh38.pl4), and the RCS gene sequence, using minimap2 v2.26 *[minimap2 - ax splice -kl4 -y -uf — secondary=no].* For transcriptome-level alignment, the reads were aligned against the human

transcriptome (v47), obtained via GENCODE (Mudge et al. 2025) *[minimap2 -t 8 -ax map-ont -y -L -p 0.99],* Using SAMtools vl.18, resulting genome- and transcriptome-aligned SAM files were converted to BAM files retaining only primary alignments *[samtools view -b -F2308* and *samtools view -b -F2324*, respectively]. BAM files were sorted *[samtools sort]* and indexed *[samtools index]*.

## Processing of RNA modification calls using Modkit

Probability distributions of the detected sites in human genome- and transcriptome-aligned reads were generated using sample-probs subcommand from Modkit v0.4.1 [sample-probs --hist --only-mapped --percentiles 0.1,0.2,0.3,0.4,0.5,0.6,0.7,0.8,0.85,0.9 -f 0.1]. For RCS reads -f value was increased to 0.25. The resulting .tsv files were imported into RStudio (v. 2024.12.1+563) and plotted using a custom R(v. 4.4.2) script (Dorado_mod_probability_distributions.R), with the following packages: dplyr (vl.1.4), ggplot2 (v3.5.1), reshape2 (vl.4.4), patchwork (vl.3.0).

To generate extended bedMethyl files with $m^6A$-modified and unmodified base counts from the reads mapping against the potential modification sites, we used Modkit pileup subcommand with the thresholds *[-filter-threshold A:0.8 -filter-threshold T:0.8 -filter-threshold C:0.8 -filter-threshold G:0.8 - motif A 0 —ref$REF]* with and without modification threshold filter *[-mod-thresholds a:0.98]* to generate our “filtered” and “unfiltered” datasets, respectively. Canonical nucleotide calls (A, C, G, U) were retained with > 80% probability scores for all modification datasets. Modification thresholds were set at 98% for $m^6A$ and 99% for all the other modifications, —*motif* was adjusted to the base for which modification status was examined, which further restricted the analysis to only the positions that matched canonical nucleotides in the reference genome. The resulting sites were further filtered according to the read number per site (> 20 reads) for all the downstream analysis.

## Gene Ontology analysis

GO analysis was performed using DAVID (Huang da et al. 2009). Genes harboring $m^6A$ sites were filtered for genes that were generally present in both datasets. Next, they were divided into NHDF-specific, HDlO.6-specific, and shared categories, and enrichment was assessed for biological processes. GO terms were considered significant at FDR < 0.05 with a minimum of 20 genes per GO term. For plotting, the top 20 GO terms that contained the highest gene numbers were extracted from the analysis of the shared gene sets.

## Analysis and visualization of modification stoichiometries and distributions

Stoichiometry distribution histograms and metaplots were generated using Rstudio and R v4.4.2 with the following libraries: data.table, patchwork, scales, tidyr, dplyr, ggplot2[4]. Access to scripts used for analysis and visualization is detailed below.

# Data availability

Raw fastq and pod5 datasets generated in this study are available via the European Nucleotide Archive (ENA) under the accession number PRJEB101380. R scripts used in the analysis and visualization of data presented herein are available in the *https://github.com/DepledgeLab/HOLDEN* repository. The Snakemake workflow implementing the GLORI analysis pipeline is available in the *https://github.com/gp-micro/glori* repository.

# Supplementary figures

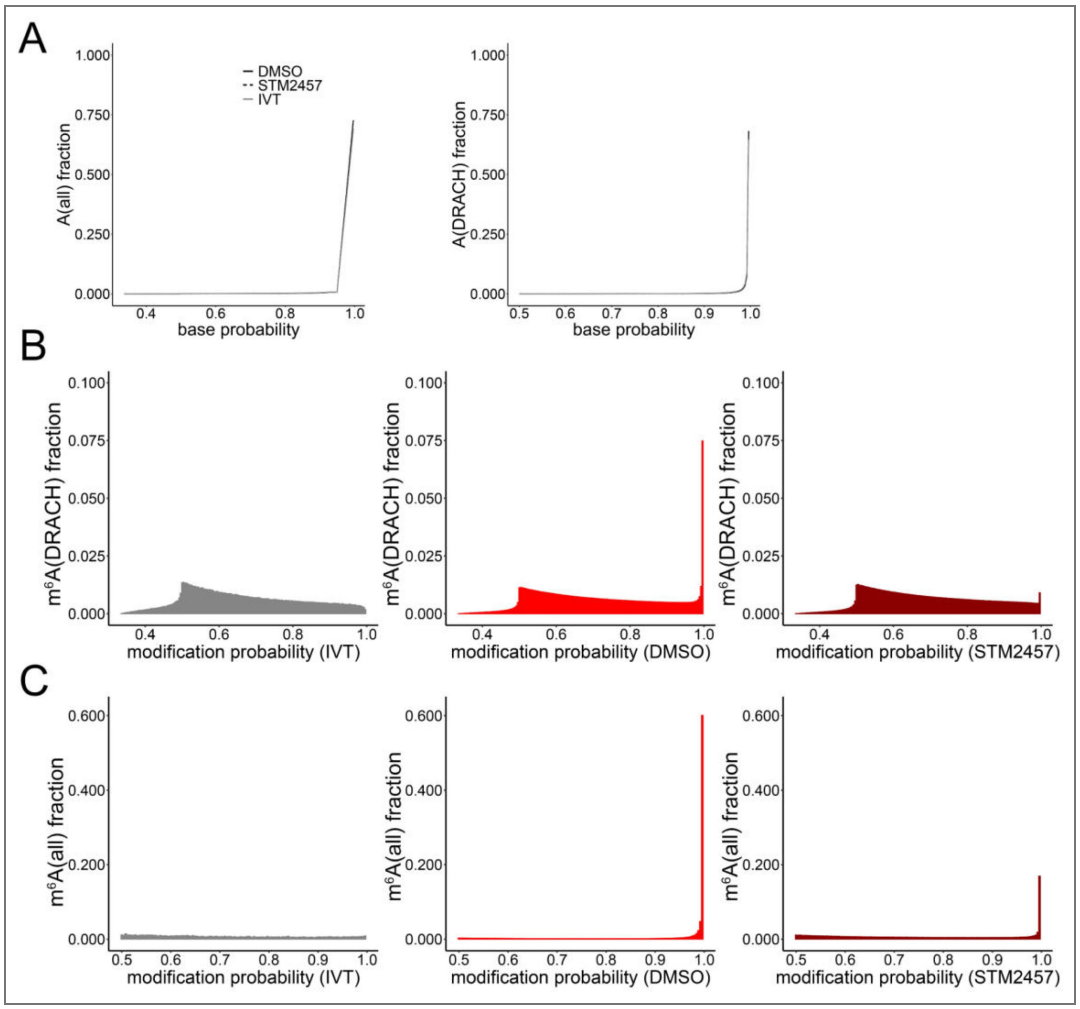


**Figure S1. Evaluation of Dorado by base and modification probability distributions. (A)** Dorado v0.9.0-generated basecall accuracy probability values for A (all-context and DRACH-context basecaller models) from genome-aligned DMSO- and STM2457-treated NHDF samples against IVT poly(A) NHDF RNA. A probability score distribution is shown as a black solid line for DMSO, STM2457 - black dashed line, IVT - grey solid line. **(B)** Dorado v0.9.0-generated modification probability distributions, visualized as histograms, for DRACH-context $m^6A$ from genome-aligned DMSO- and STM2457-treated NHDFs and IVT NHDFs. IVT modification probability score distribution is shown in grey, DMSO - bright red, STM2457 -dark red. **(C)** Same as in (B), but for all-context $m^6A$ sites.

**Figure S2. Modification probability cutoffs are necessary to identify ψ and inosine sites more accurately.**

**(A)** Dorado v0.9.0-generated basecall accuracy probability values for U (left) and modification probability distributions for ψ (right) from genome-aligned DMSO- and STM2457-treated NHDF samples are plotted against IVT poly(A) RNA. ψ probabilities are visualized in blue solid and dashed lines for DMSO and STM2457, respectively and in grey solid line for IVT. **(B)** Same as in (A) but showing A base accuracy probabilities and inosine sites. Inosine probabilities are visualized in purple solid and dashed lines for DMSO and STM2457, respectively and in grey solid line for IVT. **(C)** Same as in (A) but showing C base accuracy probabilities and $m^5C$ sites. $m^5C$ probabilities are visualized in green solid and dashed lines for DMSO and STM2457, respectively and in grey solid line for IVT. **(D+E)** DRACH-context and all-context $m^6A$ modification probability distributions (red) from genome-aligned DMSO- and STM2457-treated NHDFs are plotted against RCS negative control (grey).

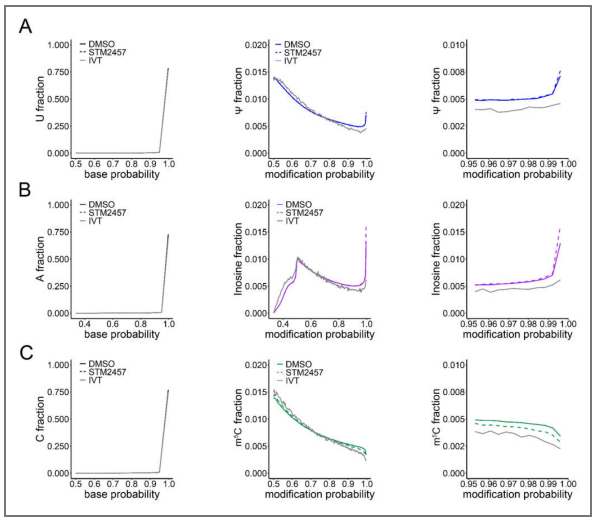


**Figure S3. Modification probability cutoffs are necessary to identify modification sites accurately, shown for transcriptome-aligned data.**

Dorado v0.9.0-generated basecall accuracy probability values for A, U and C (left, **A-E)** and modification probability distributions for $m^6A$ (all-context), $m^6A$ (DRACH-context), ψ, inosine and $m^5C$ (right, **A-E**) in transcriptome-aligned DMSO-and STM2457-treated NHDFs, plotted against the values from IVT NHDF poly(A) RNA.

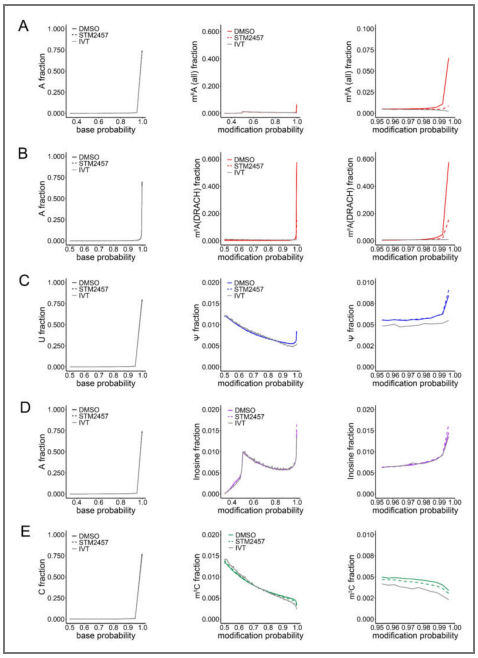

**Figure S4. Modification probability distribution profiles in genome-aligned DMSO-and STM2457-treated HD10.6 cells.**

Dorado v0.9.0-generated basecall accuracy probability values for A, U and C (left, **A-E**) and modification probability distributions for $m^6A$ (all-context), $m^6A$ (DRACH-context), ψ, inosine and $m^5C$ (right, **A-E**) in human genome-aligned DMSO- and STM2457-treated HD10.6 cells, plotted against the values from IVT NHDF poly(A) RNA.

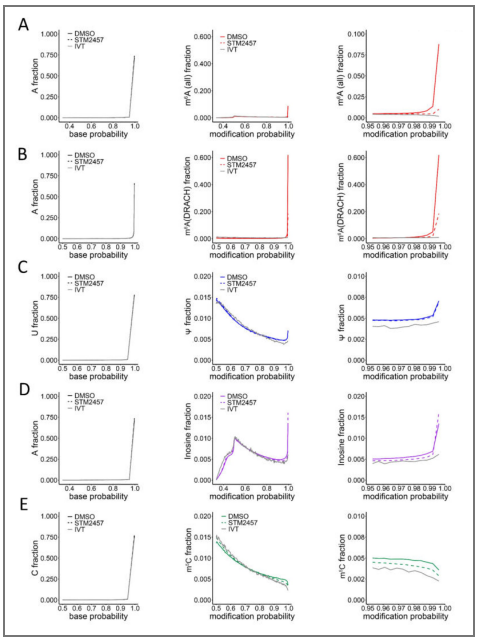


**Figure S5. Modification probability distribution profiles in transcriptome-aligned DMSO-and STM2457-treated HD10.6 cells.**

Dorado v0.9.0-generated basecall accuracy probability values for A, U and C (left, **A-E**) and modification probability distributions for $m^6A$ (all-context), $m^6A$ (DRACH-context), ψ, inosine and $m^5C$ (right, **A-E**) in human transcriptome-aligned DMSO-and STM2457-treated HD10.6 cells, plotted against the values from IVT NHDF poly(A) RNA.

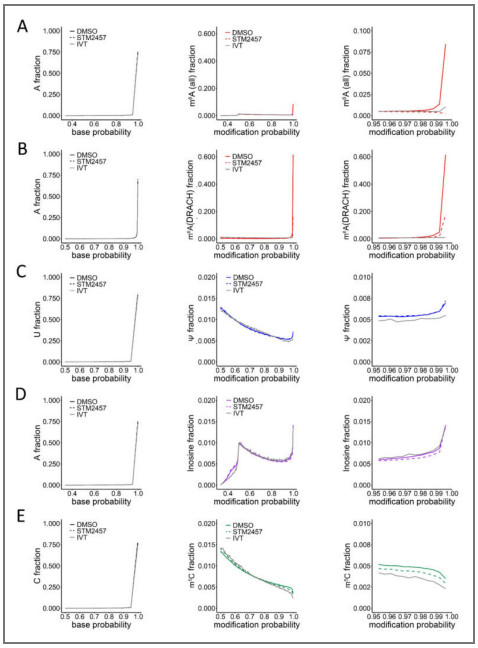

**Figure S6. Modification site probabilities detected with different versions of Dorado and compared to RCS.**

**(A+B)** DRACH-context and all-context m$^6$A modification probability distributions from genome-aligned DMSO (solid red line)- and STM2457 (dashed red line)-treated NHDFs are plotted against RCS negative control (grey). **(C)** Modification probability distributions for all-context m$^6$A (Dorado v0.7.0, v0.8.0 and v0.9.0), the bottom panel showing the distributions in 0.95-1.00 modification range. **(D)** Same as in (C), but for DRACH-context m$^6$A (Dorado v0.5.0, v0.6.0, v0.8.0 and v0.9.0). **(E)** Same as in (C), but for ψ (Dorado v0.7.0, v0.8.0, v0.9.0). All the plots in C-E are generated from genome-aligned DMSO-treated NHDF datasets and are plotted against RCS negative controls.

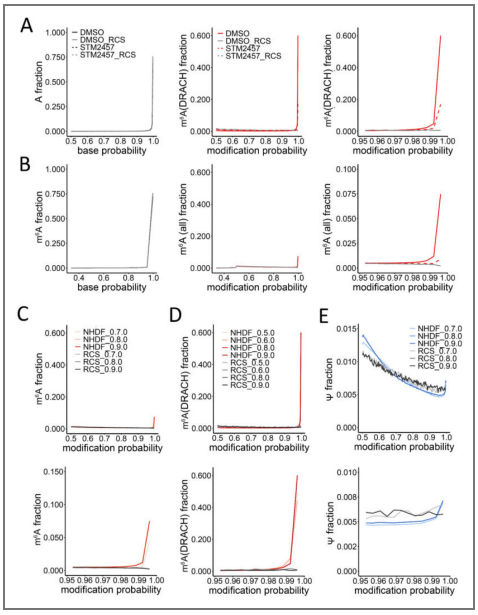


**Figure S7. Evaluation of Dorado by stoichiometry distributions.**

**(A)** Stoichiometry distributions for all-context m$^6$A from DMSO- (in red) or STM2457-treated (in pink) NHDF datasets (genome-aligned and filtered for > 20 reads) are plotted, comparing 0.98 modification probability-unfiltered (left) and filtered (right) sites. **(B)** Same as in (A), but for DRACH-context m$^6$A sites.

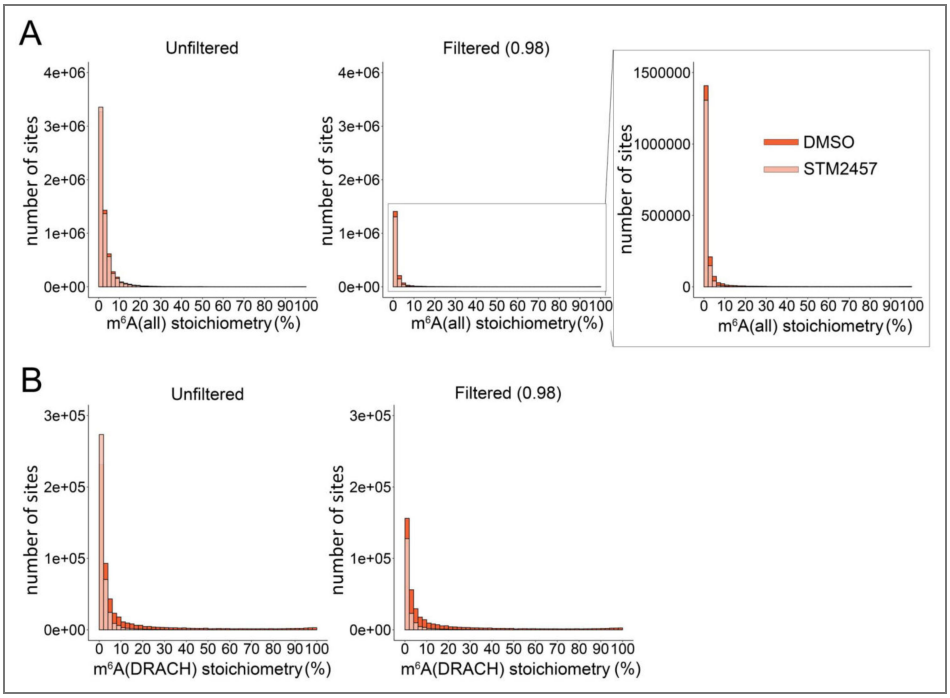

**Figure S8. Stoichiometry distributions of m$^6$A, ψ and inosine in IVT datasets.**

**(A)** All-context m$^6$A stoichiometry distributions (all stoichiometries (top) and > 10% stoichiometries (bottom)) in (genome-aligned) IVT RNA from DMSO-treated NHDFs, comparing modification probability-unfiltered and filtered data. The bottom panel shows stoichiometry distributions only for > 10% stoichiometry sites. **(B)** As in (A), but for DRACH-context m$^6$A. **(C)** As in (A), but for ψ. (D) As in (A), but for inosine.

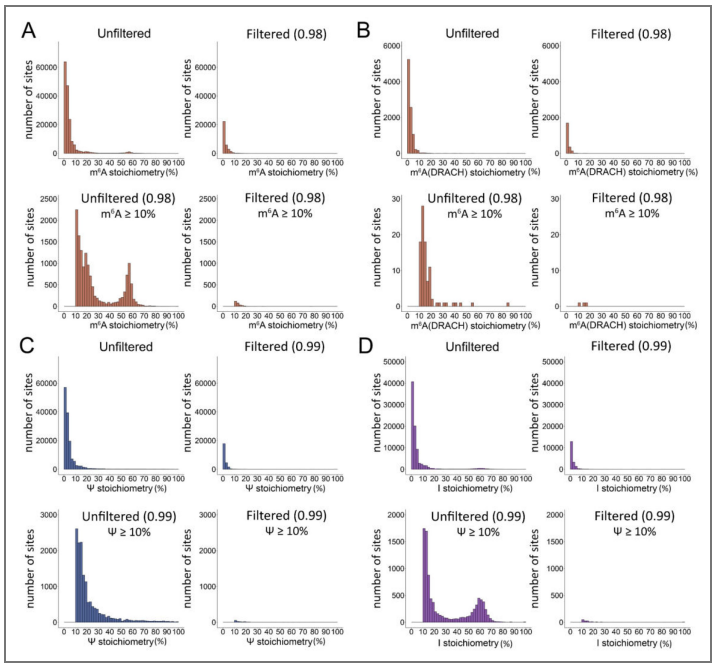


**Figure S9. Evaluation of Dorado by stoichiometry distributions in transcriptome-aligned NHDFs.**

**(A)** Stoichiometry distributions for all-context m$^{\varepsilon}$A from DMSO- (in red) or STM2457-treated (in pink) NHDF datasets (transcriptome-aligned and filtered for > 20 reads) are plotted, assessing the 0.98 modification probability cutoff. The bottom panel shows stoichiometry distributions only for > 10% stoichiometry sites. **(B)** Same as in (A), but for DRACH-context m$^6$A sites.

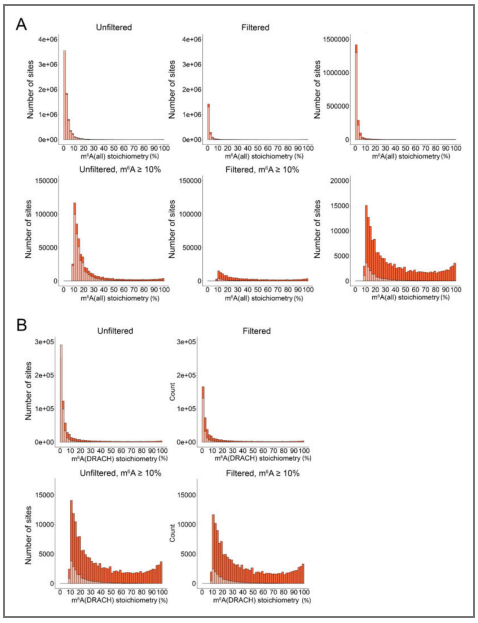

**Figure S10. Evaluation of Dorado by stoichiometry distributions in transcriptome-aligned HD10.6 cells.**

**(A)** Stoichiometry distributions for all-context m$^6$A from DMSO- (in red) or STM2457-treated (in pink) HD10.6 datasets (transcriptome-aligned and filtered for > 20 reads) are plotted, assessing the 0.98 modification probability cutoff. The bottom panel shows stoichiometry distributions only for > 10% stoichiometry sites. **(B)** Same as in (A), but for DRACH-context m$^6$A sites.

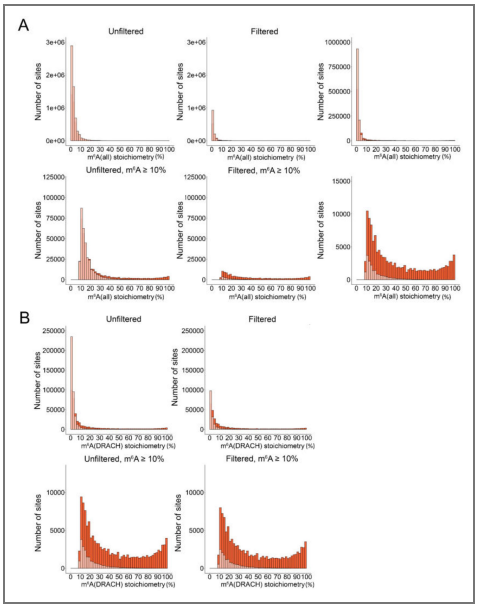


**Figure S11. Stoichiometry distributions of ψ and inosine in NHDFs.**

**(A)** Distributions of all (left) and > 10% (right) ψ stoichiometries in the 0.99 modification probability-unfiltered and filtered data from genome-aligned DMSO-(darker color) and STM2457-treated (lighter color) NHDFs (filtered for > 20 reads). (B) Same as in (A), but for inosine.

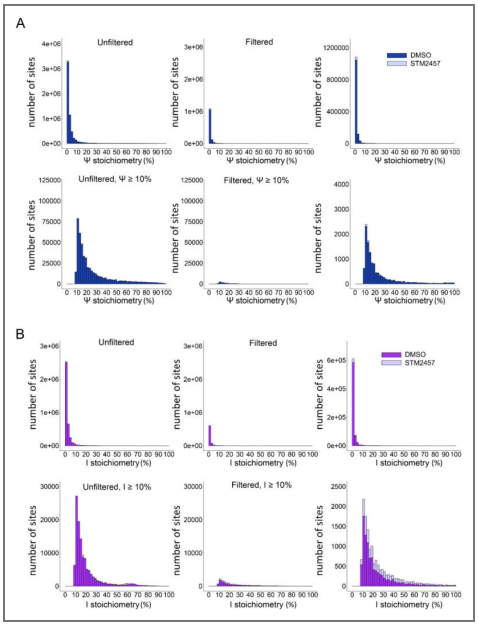

**Figure S12. Stoichiometry distributions of ψ and inosine in HD10.6 cells.**

**(A)** Distributions of all and > 10% ψ stoichiometries in the 0.99 modification probability-unfiltered and filtered data from genome-aligned DMSO-(darker color) and STM2457-treated (lighter color) HD10.6 cells (filtered for > 20 reads). **(B)** Same as in (A), but for inosine.

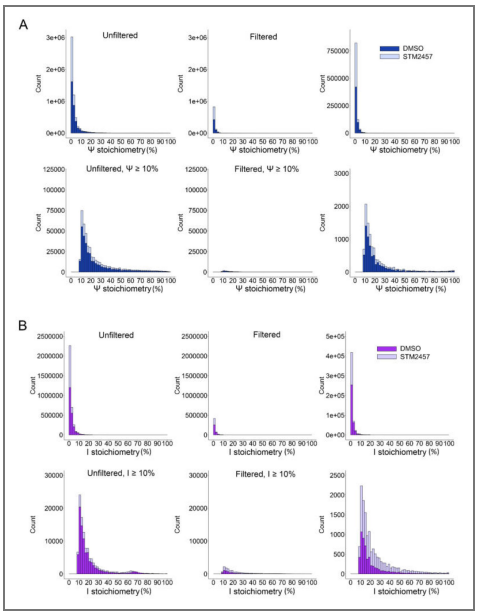


**Figure S13. m$^6$A and ψ stoichiometry distributions in different versions of Dorado.**

Stoichiometry distributions (all stoichiometries - left, > 10% stoichiometries - right) in a line graph format for (A) all-context m$^6$A detected in genome-aligned DMSO-treated NHDF dataset, with Dorado versions 0.7.0, 0.8.0 and 0.9.0 colored in gradients of red, darkness increasing with the later versions. **(B)** DRACH-context m$^6$A detected with Dorado versions 0.5.0, 0.6.0, 0.8.0 and 0.9.0, colored in gradients of red, darkness increasing with the later versions. **(C)** ψ detected with Dorado versions 0.7.0, 0.8.0 and 0.9.0, colored in gradients of blue, darkness increasing with the later versions. All the datasets were filtered for > 20 reads.

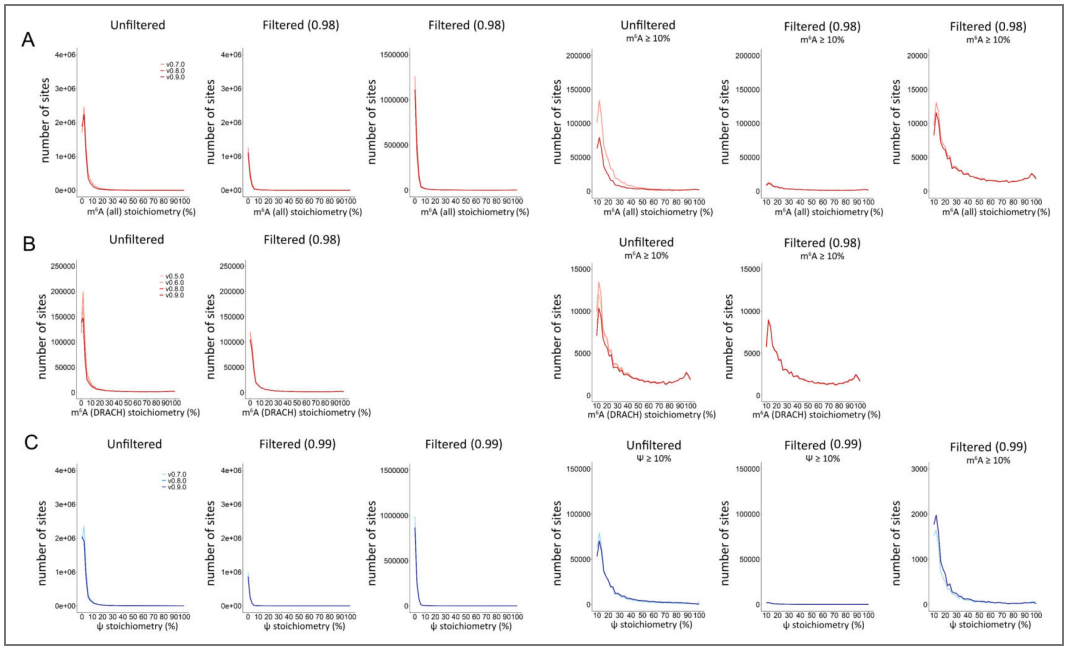

**Figure S14. Comparison of modification sites detected with different versions of Dorado.**

Upset plots showing unique and shared detected modifications (filtered for > 20 reads, > 10% stoichiometry) in modification probability-unfiltered and filtered genome-aligned DMSO-treated NHDF data. The versions are ordered on the plot by the number of detected sites, in ascending order (on the left). Results are shown for the following models and versions: **(A)** all-context $m^bA$ detected with v.0.7.0, v0.8.0 and v0.9.0, **(B)** DRACH-context $m^6A$ detected with v.0.5.0, v0.6.0, v0.8.0 and v0.9.0, **(C)** ψ detected with v.0.7.0, v0.8.0 and v0.9.0. **(D)** Nucleotide frequencies in the 5-base motif of ψ sites for uniquely v0.7.0-, v0.8.0-0.9.0- and v0.7.0-0.8.0-0.9.0-detected ψ sites. Position 0 marks the modification site.

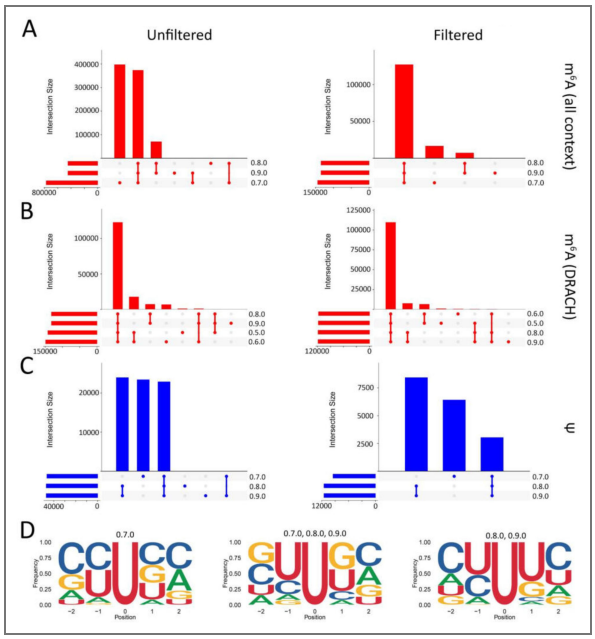


**Figure S15. Comparison of $m^6A$ sites detected by Dorado and GLORI-Sequencing in NHDFs and HDlO.6s.**

**(A)** Upset plot showing the number of $m^6A$ sites detected by GLORI and Dorado in NHDFs and their overlaps. Dorado sites represent high-confidence $m^6A$ sites obtained after filtering DRACH-model detected data. Similarly, only high confidence $m^6A$ sites detected by GLORI are shown but were additionally filtered for DRACH sites. **(B)** Stoichiometry distributions are plotted from genome-aligned DMSO- or STM2457-treated HD10.6 datasets using the indicated Dorado models. **(C)** Stoichiometry distributions from GLORI performed on DMSO- or STM2457-treated NHDFs are plotted. In addition, $m^6A$ sites were filtered for DRACH motifs (right plot). **(D)** Stoichiometry distributions are plotted from transcriptome-aligned DMSO- or STM2457-treated NHDF datasets using the indicated Dorado models. **(E)** Stoichiometry distributions are plotted from transcriptome-aligned DMSO- or STM2457-treated HD10.6 datasets using the indicated Dorado models.

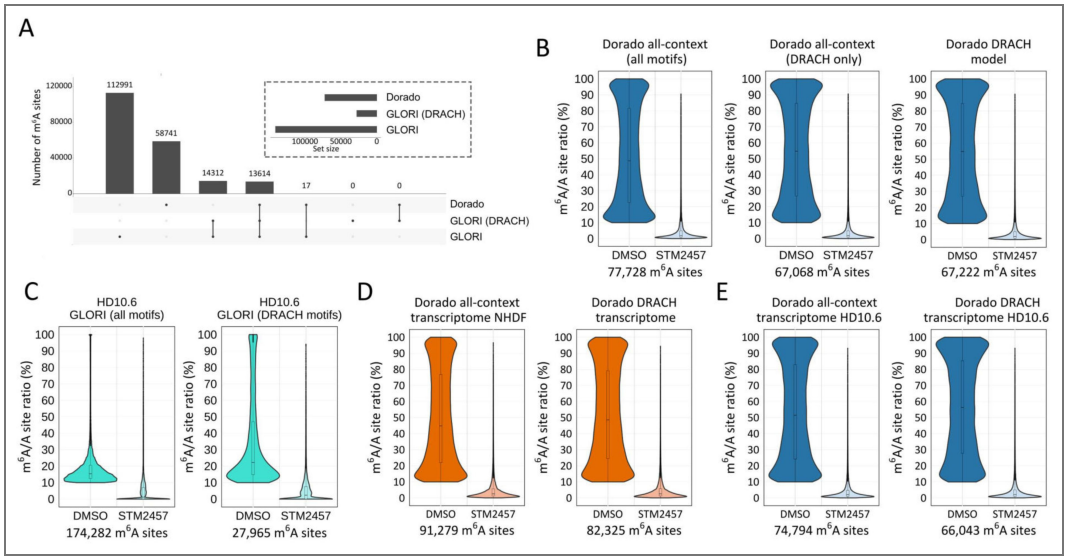

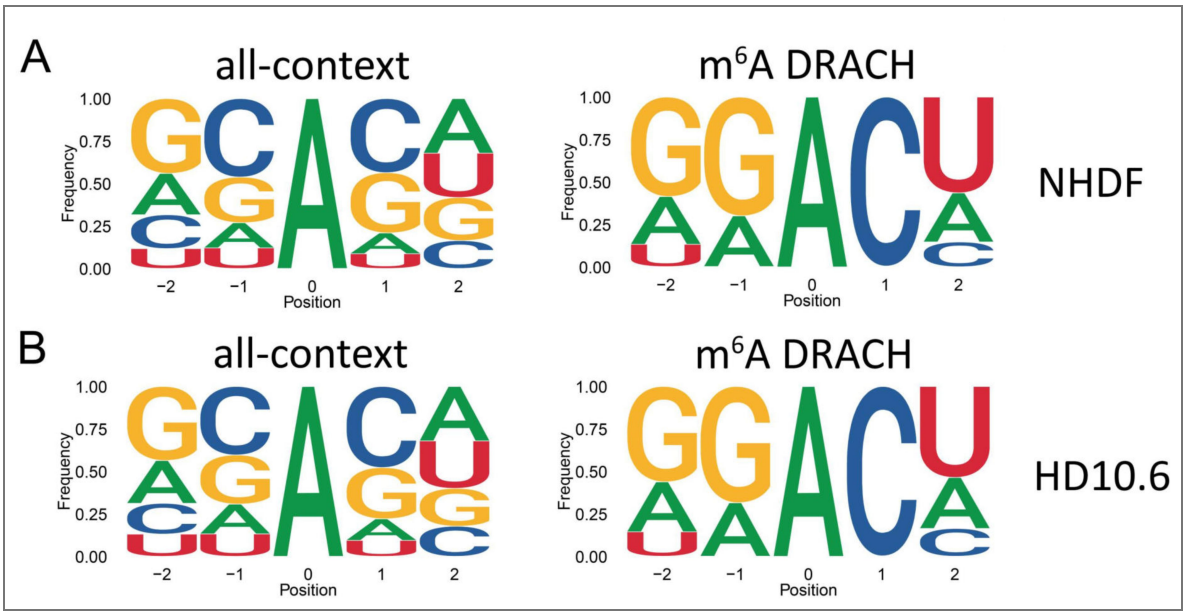


**Figure S16. m$^6$A (all-context and DRACH-context) motif logos for modification probability-unfiltered NHDF and HD10.6 data.**

**(A)** 5-mer motif logo (showing nucleotide frequences at each position) of m$^6$A-modified sites (position 0 = modified A) from genome-aligned DMSO-treated NHDFs (all-context - left, DRACH-context - right). All the datasets were filtered for > 20 coverage & > 10% stoichiometry. **(B)** Same as (A), but for HD10.6 cells.

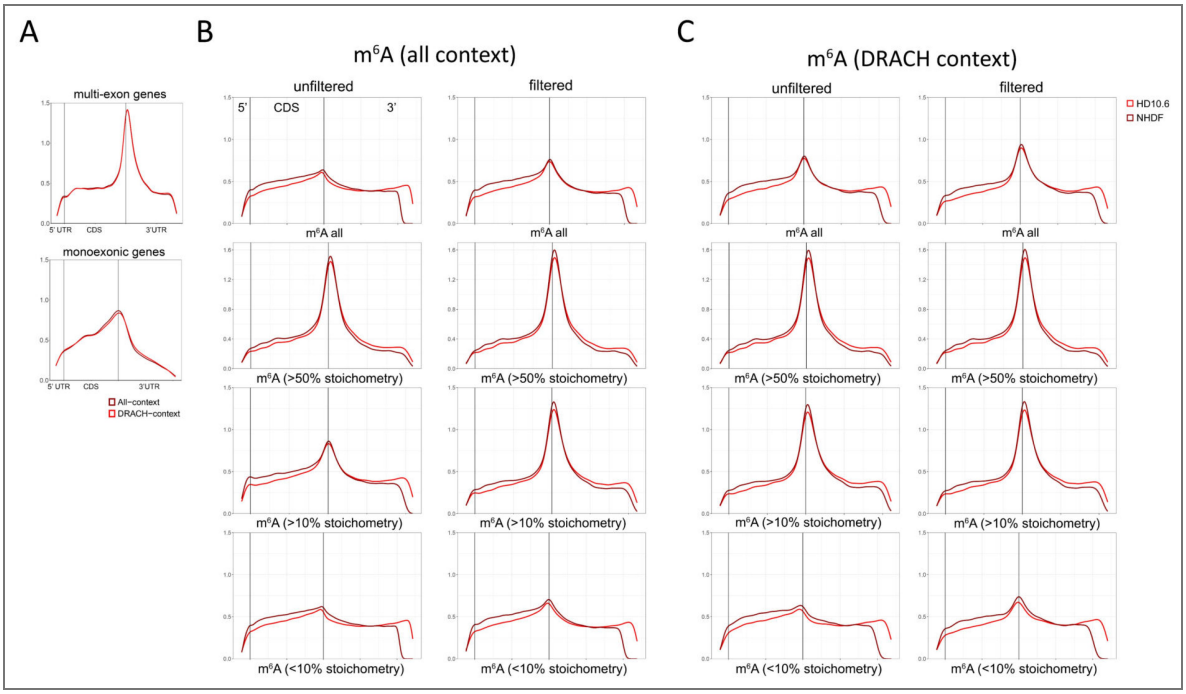


**Figure S17. Metagene plots showing m$^6$A (all-context and DRACH-context) distribution profiles in NHDF and HD10.6 data filtered at different stoichiometries.**

**(A)** Metagene plots showing the density of m$^6$A (all-context - dark red, DRACH-context - bright red) sites across all annotated poly(A) transcripts (upper plot) and monoexonic poly(A) transcripts (lower plot) from genome-aligned DMSO-treated NHDF datasets filtered with 0.98 modification probability, > 20 coverage and > 10% stoichiometry. **(B)** The density of all-context m$^6$A sites (0.98 modification probability-unfiltered - left, filtered - right) is plotted across all annotated poly(A) transcripts of NHDF (dark red) and HD10.6 (bright red) datasets, filtered with different stoichiometries (descending: all stoichiometries, > 50%, > 10% and < 10%. All datasets were filtered additionally for > 20 coverage & > 10% stoichiometry. **(C)** Same as (A), but for DRACH-context m$^6$A sites.

## Acknowledgements

DPD is supported by a German Centre for Infection Research (DZIF) Associate Professorship and the NIAID grants R01-AI170583 and R01-AI152543. DPD also receives funding from the Deutsche Forschungsgemeinschaft (DFG, German Research Foundation) under Germany's Excellence Strategy - EXC 2155, project number 390874280. EL is supported by the NIAID grant R01-AI170583 as well as the Hannover Biomedical Research School (HBRS) and the Center for Infection Biology (ZIB). DO is supported by the Walter Benjamin Programme of the DFG, project 554758329. ACW is supported by NIAID grants R01AI176335 and R01-AI170583.

## Additional files

***Supplementary Table S1.***

***Supplementary Table S2.***

***Supplementary Table S3.***

***Supplementary Table S4.***

## Additional information

### Funding


| Funder | Grant reference number |
|---|---|
| German Center for Infection Research | |
| NIAID | R01-AI170583 |
| NIAID | R01-AI152543 |
| NIAID | R01AI176335 |
| Deutsche Forschungsgemeinschaft | 390874280 |
| Deutsche Forschungsgemeinschaft | 554758329 |


### Author ORCID iDs

**Denise Ohnezeit**: https://orcid.org/0000-0002-2346-2545
**Elene Loliashvili**: https://orcid.org/0009-0006-4098-5010
**Gregory Putzel**: https://orcid.org/0000-0002-5211-2608
**Ruth Verstraten**: https://orcid.org/0009-0008-6046-6335
**Jianheng Liu**: https://orcid.org/0000-0003-0216-1951
**Luke S Nicholson**: https://orcid.org/0009-0005-8203-7249
**Alejandro Pironti**: https://orcid.org/0000-0002-7759-6776
**Samie R Jaffrey**: https://orcid.org/0000-0003-3615-6958
**Daniel P Depledge**: https://orcid.org/0000-0002-4292-0599
**Angus C Wilson**: https://orcid.org/0000-0002-5016-4164

## References

**Oxford Nanopore Technologies** (2023) Nanopore Modkit. GitHub. https://github.com/nanoporetech/modkit

**Abebe JS,** Verstraten R, Depledge DP (2022) Nanopore-Based Detection of Viral RNA Modifications. *mBio* **13**:e03702-03721 https://doi.org/10.1128/mbio.03702-21 | PubMed

**Anreiter I,** Mir Q, Simpson JT, Janga SC, Soller M (2021) New Twists in Detecting mRNA Modification Dynamics. *Trends Biotechnol* **39**:72-89 https://doi.org/10.1016/j.tibtech.2020.06.002 | PubMed

**Cappannini A,** Ray A, Purta E, Mukherjee S, Boccaletto P, Moafinejad SN, Lechner A, Barchet C, Klaholz Bruno P, Stefaniak F, *et al.* (2023) M0D0MICS: a database of RNA modifications and related information. 2023 update. *Nucleic Acids Research* **52**:D239-D244 https://doi.org/10.1093/nar/gkad1083 | PubMed

**Cruciani S,** Delgado-Tejedor A, Pryszcz LP, Medina R, Llovera L, Novoa EM (2025) De novo basecalling of RNA modifications at single molecule and nucleotide resolution. *Genome Biology* **26**:38 https://doi.org/10.1186/s13059-025-03498-6 | PubMed

**Diensthuber G,** Novoa EM (2025) Charting the epitranscriptomic landscape across RNA biotypes using native RNA nanopore sequencing. *Mol Cell* **85**:276-289 https://doi.org/10.1016/j.molcel.2024.12.014 | PubMed

**Dominissini D,** Moshitch-Moshkovitz S, Schwartz S, Salmon-Divon M, Ungar L, Osenberg S, Cesarkas K, Jacob-Hirsch J, Amariglio N, Kupiec M, *et al.* (2012) Topology of the human and mouse m6A RNA methylomes revealed by m6A-seq. *Nature* **485**:201-206 https://doi.org/10.1038/nature11112 | PubMed

**Esfahani NG,** Stein AJ, Akeson S, Tzadikario T, Jain M (2025) Evaluation of Nanopore direct RNA sequencing updates for modification detection. *bioRxiv* https://doi.org/10.1101/2025.05.01.651717 | PubMed

**Garalde DR,** Snell EA, Jachimowicz D, Sipos B, Lloyd JH, Bruce M, Pantic N, Admassu T, James P, Warland A, *et al.* (2018) Highly parallel direct RNA sequencing on an array of nanopores. *Nat Methods* **15**:201-206 https://doi.org/10.1038/nmeth.4577 | PubMed

**Gilbert WV,** Nachtergaele S (2023) mRNA Regulation by RNA Modifications. *Annu Rev Biochem* **92**:175-198 https://doi.org/10.1146/annurev-biochem-052521-035949 | PubMed

**Gleeson J,** Madugalle SU, Wan CY, McLean C, Bredy TW, De Paoli-Iseppi R, Clark MB (2025) Isoform-level profiling of m(6)A epitranscriptomic signatures in human brain. *SciAdv* **11**:eadp0783 https://doi.org/10.1126/sciadv.adp0783 | PubMed

**Guo W,** Ren Z, Huang X, Liu J, Shao J, Ma X, Wei C, Cun Y, He J, Zhang J, *et al.* (2025) Single-molecule m6A detection empowered by endogenous labeling unveils complexities across RNA isoforms. *Molecular Cell* https://doi.org/10.1016/j.molcel.2025.01.014

**He PC,** He C (2021) m(6) A RNA methylation: from mechanisms to therapeutic potential. *Embo j* **40**:el05977 https://doi.org/10.15252/embj.2020105977 | PubMed

**Hendra C,** Pratanwanich PN, Wan YK, Goh WSS, Thiery A, Göke J (2022) Detection of m6A from direct RNA sequencing using a multiple instance learning framework. *Nature Methods* **19**:1590-1598 https://doi.org/10.1038/s41592-022-01666-1 | PubMed

**Hewel C,** Wierczeiko A, Miedema J, Friedrich J, Hofmann F, Weiβbach S, Dietrich V, Holthöfer L, Haug V, Mündnich S, *et al.* (2025) Direct RNA sequencing enables improved transcriptome assessment and tracking of RNA modifications for medical applications. *Nucleic Acids Research* **53** https://doi.org/10.1093/nar/gkaf1314 | PubMed

**Huang da W,** Sherman BT, Lempicki RA (2009) Systematic and integrative analysis of large gene lists using DAVID bioinformatics resources. *Nat Protoc* **4**:44-57 https://doi.org/10.1038/nprot.2008.211 | PubMed

**Jain M,** Olsen HE, Paten B, Akeson M (2016) The Oxford Nanopore MinION: delivery of nanopore sequencing to the genomics community. *Genome Biology* **17**:239 https://doi.org/10.1186/s13059-016-1103-0 | PubMed

**Koster J,** Rahmann S (2012) Snakemake—a scalable bioinformatics workflow engine. *Bioinformatics* **28**:2520-2522 https://doi.org/10.1093/bioinformatics/bts480 | PubMed

**Li H,** Handsaker B, Wysoker A, Fennell T, Ruan J, Homer N, Marth G, Abecasis G, Durbin R (2009) The Sequence Alignment/Map format and SAMtools. *Bioinformatics* **25**:2078-2079 https://doi.org/10.1093/bioinformatics/btp352 | PubMed

**Linder B,** Grozhik AV, Olarerin-George AO, Meydan C, Mason CE, Jaffrey SR (2015) Single-nucleotide-resolution mapping of m6A and m6Am throughout the transcriptome. *Nature Methods* **12**:767-772 https://doi.org/10.1038/nmeth.3453 | PubMed

**Liu C,** Sun H, Yi Y, Shen W, Li K, Xiao Y, Li F, Li Y, Hou Y, Lu B, *et al.* (2023) Absolute quantification of single-base m(6)A methylation in the mammalian transcriptome using GLORI. *Nat Biotechnol* **41**:355-366 https://doi.org/10.1038/s41587-022-01487-9 | PubMed

**Liu JF,** Hawley BR, Nicholson LS, Jaffrey SR (2025) Decoding m(6)Am by simultaneous transcription-start mapping and methylation quantification. *eLife* **13** https://doi.org/10.7554/elife.104139.3

**Meyer KD** (2019) DART-seq: an antibody-free method for global m6A detection. *Nature Methods* **16**:1275-1280 https://doi.org/10.1038/s41592-019-0570-0 | PubMed

**Meyer KD,** Saletore Y, Zumbo P, Elemento O, Mason Christopher E, Jaffrey Sarnie R. (2012) Comprehensive Analysis of mRNA Methylation Reveals Enrichment in 3' UTRs and near Stop Codons. *Cell* **149**:1635-1646 https://doi.org/10.1016/j.cell.2012.05.003 | PubMed

**Moshitch-Moshkovitz S,** Sevilla-Sharon M, Ashwal-Fluss R, Glick-Saar E, Rechavi G, Dominissini D (2024) mRNA m6A detection. *Nature Reviews Methods Primers* **4** https://doi.org/10.1038/s43586-024-00365-9

**Mudge JM,** Carbonell-Sala S, Diekhans M, Martinez JG, Hunt T, Jungreis I, Loveland JE, Aman C, Barnes I, Bennett R, *et al.* (2025) GENCODE 2025: reference gene annotation for human and mouse. *Nucleic Acids Res* **53**:D966-d975 https://doi.org/10.1093/nar/gkae1078 | PubMed

**Murakami S,** Jaffrey SR (2022) Hidden codes in mRNA: Control of gene expression by m(6)A. *Mol Cell* **82**:2236-2251 https://doi.org/10.1016/j.molcel.2022.05.029 | PubMed

**Raymon HK,** Thode S, Zhou J, Friedman GC, Pardinas JR, Barrere C, Johnson RM, Sah DWY (1999) Immortalized Human Dorsal Root Ganglion Cells Differentiate into Neurons with Nociceptive Properties. *The Journal of Neuroscience* **19**:5420-5428 https://doi.org/10.1523/jneurosci.19-13-05420.1999 | PubMed

**Sendinc E,** Shi Y (2023) RNA m6A methylation across the transcriptome. *Mol Cell* **83**:428-441 https://doi.org/10.1016/j.molcel.2023.01.006 | PubMed

**Shen W,** Sun H, Liu C, Yi Y, Hou Y, Xiao Y, Hu Y, Lu B, Peng J, Wang J, *et al.* (2024) GLORI for absolute quantification of transcriptome-wide m6A at single-base resolution. *Nature Protocols* **19**:1252-1287 https://doi.org/10.1038/s41596-023-00937-1 | PubMed

**Su C-H D D,** Tarn W-Y (2018) Alternative Splicing In Neurogenesis and Brain Development. *Frontiers in Molecular Biosciences* **5** https://doi.org/10.3389/fmolb.2018.00012 | PubMed

**Sun H,** Li K, Liu C, Yi C (2023) Regulation and functions of non-m(6)A mRNA modifications. *Nat Rev Mol Cell Biol* **24**:714-731 https://doi.org/10.1038/s41580-023-00622-x | PubMed

**Sun H,** Lu B, Zhang Z, Xiao Y, Zhou Z, Xi L, Li Z, Jiang Z, Zhang J, Wang M, *et al.* (2025) Mild and ultrafast GLORI enables absolute quantification of m6A methylome from low-input samples. *Nature Methods* **22**:1226-1236 https://doi.org/10.1038/s41592-025-02680-9 | PubMed

**Verstraten R,** Cetraro P, Fitzpatrick AH, Alwie Y, Frommeyer YN, Loliashvili E, Stein SC, Häussler S, Ouwendijk WJD, Depledge DP (2025) Defining expansions and perturbations to the RNA polymerase III transcriptome and epitranscriptome by modified direct RNA nanopore sequencing. *bioRxiv* https://doi.org/10.1101/2025.03.07.641986 | PubMed

**Viehweger A,** Krautwurst S, Lamkiewicz K, Madhugiri R, Ziebuhr J, Hölzer M, Marz M (2019) Direct RNA nanopore sequencing of full-length coronavirus genomes provides novel insights into structural variants and enables modification analysis. *Genome Res* **29**:1545-1554 https://doi.org/10.1101/gr.247064.118 | PubMed

**Xiao YL,** Liu S, Ge R, Wu Y, He C, Chen M, Tang W (2023) Transcriptome-wide profiling and quantification of N(6)-methyladenosine by enzyme-assisted adenosine deamination. *Nat Biotechnol* **41**:993-1003 https://doi.org/10.1038/s41587-022-01587-6 | PubMed

**Xie YY,** Zhong ZD, Chen HX, Ren ZH, Qiu YT, Lan YL, Wu F, Kong JW, Luo RJ, Zhang D, *et al.* (2025) Single-molecule direct RNA sequencing reveals the shaping of epitranscriptome across multiple species. *Nat Commun* **16**:5119 https://doi.org/10.1038/s41467-025-60447-4 | PubMed

**Xu H,** Kong L, Cheng J, Al Moussawi K, Chen X, Iqbal A, Wing PAC, Harris JM, Tsukuda S, Embarc-Buh A, *et al.* (2024) Absolute quantitative and base-resolution sequencing reveals comprehensive landscape of pseudouridine across the human transcriptome. *Nature Methods* **21**:2024-2033 https://doi.org/10.1038/s41592-024-02439-8 | PubMed

**Yang L,** Tang L, Min Q, Tian H, Li L, Zhao Y, Wu X, Li M, Du F, Chen Y, *et al.* (2024a) Emerging role of RNA modification and long noncoding RNA interaction in cancer. *Cancer Gene Ther* **31**:816-830 https://doi.org/10.1038/s41417-024-00734-2 | PubMed

**Yang Y,** Lu Y, Wang Y, Wen X, Qi C, Piao W, Jin H (2024b) Current progress in strategies to profile transcriptomic m(6)A modifications. *Front Cell Dev Biol* **12**:1392159 https://doi.org/10.3389/fcell.2024.1392159 | PubMed

**Yankova E,** Blackaby W, Albertella M, Rak J, De Braekeleer E, Tsagkogeorga G, Pilka ES, Aspris D, Leggate D, Hendrick AG, *et al.* (2021) Small-molecule inhibition of METTL3 as a strategy against myeloid leukaemia. *Nature* **593**:597-601 https://doi.org/10.1038/s41586-021-03536-w | PubMed

**Yu J,** She Y, Ji S-J (2021) m6A Modification in Mammalian Nervous System Development, Functions, Disorders, and Injuries. . *Frontiers in Cell and Developmental Biology* **9** https://doi.org/10.3389/fcell.2021.679662 | PubMed

**Zaccara S,** Ries RJ, Jaffrey SR (2019) Reading, writing and erasing mRNA methylation. *Nature Reviews Molecular Cell Biology* **20**:608-624 https://doi.org/10.1038/s41580-019-0168-5 | PubMed

**Zou Y,** Ahsan MU, Chan J, Meng W, Gao S-J, Huang Y, Wang K (2025) A comparative evaluation of computational models for RNA modification detection using nanopore sequencing with RNA004 chemistry. *Briefings in Bioinformatics* **26** https://doi.org/10.1093/bib/bbaf404 | PubMed

# Peer reviews

## Reviewer #1 (Public review):

Summary:

The authors set out to evaluate how accurately direct sequencing of RNA can identify and quantify several chemical modifications on RNA molecules, focusing primarily on m6A. A central goal of the work is to compare this approach with an independent chemical-based method (glyoxal and nitrite-mediated deamination of unmethylated adenosines (GLORI), using the same RNA samples, in order to assess reproducibility, false-positive signals, and sensitivity across a range of detection strategies. The authors further aim to demonstrate the biological utility of this approach by applying it to two human cell types, primary human fibroblasts and HD10.6 neurons. While the manuscript also reports detection of additional RNA modifications (pseudouridine and m5C, the depth of analysis and strength of controls are greatest for m6A, which forms the primary focus of the study

Strengths:

A strength of this work is the direct comparison of two distinct measurement approaches performed on the same RNA input material; this has not been done in other recently published benchmarking studies evaluating the utility of the recent direct RNA sequencing for calling m6A. The authors systematically test multiple analysis models and show that, when appropriate filtering is applied, detection of modified sites is reproducible across software versions. The use of synthetic RNA standards and METTL3 inhibitors as negative controls helps to reinforce the overall results.

The data show good agreement between the two methods at higher m6A modification levels, supporting the conclusion that direct RNA sequencing can reliably detect high-confidence modification sites. The authors also demonstrate that this approach can, in principle, provide information at the level of individual RNA variants (although only one example was provided), which is difficult to achieve with short-read methods. The methodology described here is likely to be useful to others seeking to apply similar approaches to identify and quantify m6A. The study also explores the detection of other RNA modifications, which highlights the broader potential of the approach, although these analyses are necessarily more exploratory given the more limited controls and data available.

Weaknesses:

Despite these strengths, several issues limit the interpretation of the results and should be clarified for readers.

First, the authors appropriately address false-positive signals by estimating expected false-positive rates and by quantitatively comparing sequence motif enrichment before and after filtering. These analyses provide important support for the use of stoichiometry-based thresholds and demonstrate that filtering substantially improves specificity. However, even after filtering, a subset of detected sites remains outside the expected sequence context. It therefore remains unclear to what extent these non-canonical sites reflect genuine biology versus residual technical artifacts.

Second, claims regarding the ability of direct RNA sequencing to resolve modification patterns across different RNA variants are supported by very limited evidence. The conclusion that this approach provides superior isoform-level quantification relative to short-read methods is based largely on a single gene example. While this case is interesting, it does not establish how widespread or general this advantage is. A broader analysis indicating how many genes show isoform-specific modification patterns detectable by this method, and how often these are missed by the comparison approach, would be necessary to support a general claim.

Third, the biological interpretation of cell type-specific differences in modification levels remains underdeveloped. Although differences in modification stoichiometry are reported between fibroblasts and neuron-derived cells, the functional consequences of these differences are not addressed. It is unclear whether changes in modification levels are associated with differences in RNA abundance, stability, or translation. As a result, statements suggesting that these modifications fine-tune core cellular pathways are speculative and should either be supported with additional analyses or framed more cautiously.

Related to this point, differences in gene expression between the two cell types are a potential confounding factor. The pathway enrichment patterns presented appear biased toward particular functional categories, but without clear control for differential gene expression, it is difficult to determine whether the observed enrichment reflects cell type-specific regulation of RNA modification or simply differences in which genes are expressed. Clarifying how background gene sets were defined for these analyses would help readers interpret the results.

The manuscript also suggests broader differences in overall modification levels between cell types, but this is not validated using an independent global assay. An orthogonal measurement of total modification levels on polyadenylated RNA (for example, dot blot) would help place site-specific stoichiometry differences in a clearer biological context.

Finally, the effects of the METTL3 inhibitor on these cell types are not fully characterized. While changes in m6A modification patterns are reported following treatment, the manuscript does not address whether the treatment affects cell growth or viability.

Appraisal of conclusions and impact:

Overall, the study provides an informative technical assessment of direct RNA sequencing for modification detection and establishes clear conditions under which the method performs well. The evidence strongly supports conclusions related to technical benchmarking, reproducibility, and the importance of filtering and controls, particularly for m6A. In contrast, conclusions regarding isoform-specific regulation and cell type-specific biological roles of RNA modification are less well supported by the data currently presented, and would benefit from either additional analysis or more restrained interpretation.

The work is likely to have a meaningful impact as a practical reference for researchers using direct RNA sequencing, particularly by clarifying sources of false positives and the value of appropriate controls. With clearer limits placed on biological interpretation or more data presented in support of the biological interpretation, the study would serve as a valuable reference for users seeking to apply these technologies reliably.

https://doi.org/10.7554/eLife.110672.1.sa2

## Reviewer #2 (Public review):

Summary:

In this study, the authors aim to establish a calibrated framework for detecting RNA modifications using long-read sequencing and apply it to compare modification patterns between fibroblasts and neuron-like cells. The work combines long-read sequencing, in vitro transcribed controls, methyltransferase inhibition, and comparison to an orthogonal sequencing-based method in an attempt to derive filtering strategies that reduce false positive modification calls. The authors further apply this framework to explore differences in modification levels between the two cell types.

The resulting dataset may be of interest to researchers working on RNA modification detection using long-read sequencing technologies. Independent datasets across additional cellular systems can be useful for benchmarking computational methods and evaluating the behavior of modification detection models. However, the conceptual advance of the analytical framework presented here remains somewhat unclear, as many aspects of the analysis closely resemble strategies that have already been described in recent benchmarking studies.

Strengths:

A clear strength of the study is the generation of a relatively large long-read sequencing dataset together with several useful experimental controls, including in vitro transcribed RNA and pharmacological inhibition of the methyltransferase enzyme responsible for installing this modification. These controls are helpful for illustrating the challenges associated with distinguishing high-confidence modification sites from background signals. The inclusion of two different human cellular systems also provides an additional dataset that may be useful for benchmarking and cross-validation in the field. The study addresses a practically relevant question for the community, namely, how to reduce false positive calls in long-read sequencing-based RNA modification analyses.

Weaknesses:

The main weakness of the manuscript is its limited methodological novelty. Much of the analytical framework presented here closely follows benchmarking strategies that have already been described in recent studies of RNA modification detection using long-read sequencing. Several previous studies have evaluated modification-aware basecalling approaches, discussed the need for stringent filtering strategies, and compared long-read

sequencing-based predictions with orthogonal mapping approaches. The manuscript would therefore benefit from a deeper engagement with the recent benchmarking literature and a clearer explanation of what conceptual or methodological advance the present study provides beyond these earlier analyses.

A second concern relates to the filtering strategy that forms the core of the proposed workflow. The manuscript applies several thresholds, including modification probability, stoichiometry, and read coverage cutoffs, but it is not clearly explained how these thresholds were determined. It remains unclear whether these cutoffs were derived from statistical calibration, empirical optimization using the presented dataset, or adopted from previous studies. Because the downstream conclusions depend strongly on these filtering choices, a clearer methodological justification would strengthen the work and help readers assess the robustness of the proposed framework.

The interpretation of the comparison between the two modification detection approaches also appears somewhat overstated. Differences between the methods are frequently interpreted as evidence that one approach produces large numbers of false positive calls, but the analyses presented do not fully exclude alternative explanations such as differences in sensitivity, sequencing depth, or methodological biases. A more cautious interpretation of these discrepancies would therefore be appropriate.

Some discussion points also appear speculative. In particular, certain interpretations propose mechanistic explanations without presenting analyses that would allow these possibilities to be distinguished. Such interpretations would benefit from either additional supporting analyses or more cautious phrasing.

From a methodological perspective, the statistical robustness of the thresholds used throughout the analysis could also be discussed in more detail. Given the relatively modest read coverage cutoff applied in the study, low stoichiometry estimates may be strongly influenced by sampling noise, and fixed stoichiometry thresholds may therefore not correspond to a consistent level of confidence across sites. In addition, the manuscript relies heavily on fixed modification probability cutoffs to define high-confidence calls, but it does not discuss whether these scores are statistically calibrated or how they relate to expected error rates. Neural network outputs are often not well-calibrated probabilities, and interpreting these values as direct confidence estimates can therefore be problematic. Finally, modification detection models trained on known modification sites may capture sequence-context patterns present in the training data, meaning that motif enrichment or positional distributions along transcripts may partly reflect model biases rather than purely biological signals. A brief discussion of these limitations would help readers better interpret the robustness of the proposed filtering strategy and the downstream biological conclusions.

Overall, while the dataset may be of interest to the community, the extent to which the study advances current methodological understanding beyond recent benchmarking efforts remains limited.

Minor comments:

The discussion of the "DRACH" versus "all-context" outputs would benefit from greater technical precision. The statement that the number of sites within DRACH motifs identified by the all-context approach was nearly identical to the number reported by the DRACH model may suggest that these outputs derive from fundamentally different predictive models. As I understand it, the underlying neural network is the same, whereas the distinction lies primarily in the classification context. Clarifying this explicitly in the manuscript would improve interpretability and avoid potential confusion for readers.

The manuscript compares results obtained with different basecalling and modification

settings but refers primarily to Dorado software versions. This may be misleading, as software version and model version are not necessarily equivalent. Different basecalling or modification models can be used with the same software release, and newer software versions may still use older models. For clarity and reproducibility, the authors should report the exact basecalling and modification model names used in the analyses rather than referring only to the Dorado software version.

https://doi.org/10.7554/eLife.110672.1.sa1

## Reviewer #3 (Public review):

In this study, the authors aim to establish a calibrated framework for identifying RNA chemical marks from direct RNA sequencing data using a modification-aware basecalling workflow, with a particular focus on N6-methyladenosine. By combining native RNA sequencing with an unmodified control transcriptome, enzyme inhibition, comparison across multiple software versions, and orthogonal validation using an independent mapping approach, the authors seek to define a best-practice pipeline for reducing false-positive calls and improving confidence in quantitative interpretation across cell types.

A major strength of the work is the rigor of the benchmarking strategy. In particular, the inclusion of an unmodified control transcriptome is both important and useful, and the study provides compelling evidence that this control remains necessary for robust interpretation, despite being omitted in many current workflows. The comparison across software versions and the matched analysis with an independent sequencing-based approach also substantially strengthen the evidence presented. The work therefore makes a valuable contribution to the community by offering a more stringent analytical framework that will likely be broadly useful to groups applying native RNA sequencing to study RNA chemical marks.

The evidence supporting the main conclusions is solid overall. The authors convincingly show that stringent filtering substantially reduces false-positive calls and improves agreement with orthogonal approaches, particularly at highly modified sites. The observation that many sites are conserved across cell types, while showing differences in relative modification levels, is also supported by the presented analyses.

At the same time, several conceptual issues limit the strength of some downstream interpretations. Most importantly, the manuscript repeatedly refers to the reported values as "stoichiometry," whereas the underlying software output is more appropriately interpreted as a statistical estimate of the proportion of aligned reads classified as modified. This distinction is important because the conclusions regarding cell-type differences rely on quantitative comparisons of these values. In addition, the current calling framework depends on successful canonical base assignment before modification calling, which raises an important limitation: sites with the strongest signal deviations may be underrepresented if they are more likely to be miscalled during basecalling. This issue may be especially relevant for RNA marks that induce stronger mismatch signatures than N6-methyladenosine and should be more explicitly discussed.

Overall, the authors largely achieve their primary aim of establishing a more rigorous and broadly applicable analytical framework for direct RNA sequencing-based modification detection. The work is likely to have a meaningful impact on the field, particularly by reinforcing the importance of appropriate negative controls and benchmarking standards. With clearer framing of the quantitative outputs and explicit discussion of current software limitations, this study will serve as a highly useful resource for the community.

https://doi.org/10.7554/eLife.110672.1.sa0